

# Compact Radio Sources within 30'' of Sgr A\*: Proper Motions, Stellar Winds and the Accretion Rate onto Sgr A\*

F. Yusef-Zadeh<sup>1</sup>, H. Bushouse<sup>2</sup>, R. Schödel<sup>3</sup>, M. Wardle<sup>4</sup>, W. Cotton<sup>5</sup>,  
D. A. Roberts<sup>1</sup>, F. Nogueras-Lara<sup>3</sup> & E. Gallego-Cano<sup>3</sup>

<sup>1</sup>*Department of Physics and Astronomy and CIERA, Northwestern University, Evanston, IL 60208*

<sup>2</sup>*Space Telescope Science Institute, Baltimore, MD 21218*

<sup>3</sup>*Instituto de Astrofísica de Andalucía (CSIC), Glorieta de la Astronomía S/N, 18008 Granada*

<sup>4</sup>*Department of Physics and Astronomy, Macquarie University, Sydney NSW 2109, Australia*

<sup>5</sup>*National Radio Astronomy Observatory, Charlottesville, VA 22903*

## ABSTRACT

Recent broad-band 34 and 44 GHz radio continuum observations of the Galactic center have revealed 41 massive stars identified with near-IR counterparts, as well as 44 protoplanetary candidates within 30'' of Sgr A\*. Radio observations obtained in 2011 and 2014 have been used to derive proper motions of eight young stars near Sgr A\*. The accuracy of proper motion estimates based on near-IR observations by Lu et al. and Paumard et al. have been investigated by using their proper motions to predict the 2014 epoch positions of near-IR stars and comparing the predicted positions with those of radio counterparts in the 2014 radio observations. Predicted positions from Lu et al. show an rms scatter of 6 mas relative to the radio positions, while those from Paumard et al. show rms residuals of 20 mas, which is mainly due to uncertainties in the IR-based proper motions. Under the assumption of homogeneous ionized winds, we also determine the mass-loss rates of 11 radio stars, finding rates that are on average  $\sim 2$  times smaller than those determined from model atmosphere calculations and near-IR data. Clumpiness of ionized winds would reduce the mass loss rate of WR and O stars by additional factors of 3 and 10, respectively. One important implication of this is a reduction in the expected mass accretion rate onto Sgr A\* from stellar winds by nearly an order of magnitude to a value of  $\text{few} \times 10^{-7} M_{\odot} \text{ yr}^{-1}$ . Finally, we present the positions of 318 compact 34.5 GHz radio sources within 30'' of Sgr A\*. At

least 45 of these have stellar counterparts in the near-IR  $K_s$  ( $2.18\ \mu\text{m}$ ) and  $L'$  ( $3.8\ \mu\text{m}$ ) bands. The presence of a large number of compact radio sources suggests that high-frequency radio continuum observations of the Galactic center can not only characterize the properties of diffuse ionized gas, but also reveal the massive OB and WR stars, low and high mass young stellar objects and nonthermal sources, such as the magnetar SGR 1745-29, located within one parsec of Sgr A\*.

*Subject headings:* accretion, accretion disks — black hole physics — Galaxy: center

## 1. Introduction

The nuclear region of our Galaxy coincides with a stellar cluster consisting of a mixture of an evolved stellar population and a young stellar population centered on the  $4 \times 10^6\ M_\odot$  black hole Sgr A\* (Reid and Brunthaler 2004; Ghez *et al.* 2005; Gillessen *et al.* 2009). The young stellar cluster lies mainly within 1 to  $10''$  (0.04 to 0.4 pc) of the strong radio source Sgr A\*, whereas the evolved cluster has a half-light radius of  $1.8'$  ( $\sim 4.2$  pc) centered on Sgr A\* (Schödel *et al.* 2014; Fritz *et al.* 2014). The young population consists of about one hundred young massive OB and WR stars, which are contained within one or two disk-like distributions (Paumard *et al.* 2006; Lu *et al.* 2009).

Until recently, young stars in the two stellar disks could only be identified and studied using adaptive optic observations in the near-IR (NIR). These observations, however, are not able to detect a steady component of the emission from the black hole. Thus the relative position of stars with respect to the stationary black hole can not be determined directly. Radio images, on the other hand, show the bright radio source Sgr A\* and the ionized gas orbiting the black hole. The combination of radio and NIR observations are therefore needed to make accurate astrometric measurements of the various nuclear populations. The key question that accurate astrometry can address is to make accurate determinations of the positions, and hence reducing the errors and uncertainties in the positions of NIR-identified stars, such as S2, as they orbit Sgr A\*. S2 has been observed over two decades and lies  $\sim 0.2''$  from Sgr A\* with an orbital period of 15.8 years. A prograde periastron shift of  $0.2^\circ$  per one revolution around Sgr A\* is estimated to yield a positional shift of  $\sim 0.8$  mas with respect to the previous orbit (Rubilar and Eckart 2001). Thus, the accurate position of S2 with respect to Sgr A\* has important implications for probing the curvature of space-time in the context of general relativity.

To compare radio and NIR images, the accurate position of the black hole with respect to stars is determined by aligning radio and NIR frames using SiO masers. These masers are associated with members of the evolved stellar cluster and are distributed more than  $7''$  from Sgr A\* (Menten *et al.* 1997; Reid *et al.* 2003). We recently reported detection of 41 radio sources (Yusef-Zadeh *et al.* 2014a). A comparison with NIR images of similar resolution taken at the same epoch identified all radio sources having L-band ( $3.8\ \mu\text{m}$ ) counterparts (Yusef-Zadeh *et al.* 2014a). Several young, massive stars of the central cluster within a few

arcseconds of Sgr A\*, such as IRS 16C, IRS 16NE, IRS 16SE2, IRS 16NW, IRS 16SW, AF, AFNW, IRS 34W and IRS 33E, are detected in the 44 GHz observations. Most of these massive stars show P-Cygni profiles, which is strong evidence for stellar winds (Martins *et al.* 2007). We determined the mass-loss rates of individual radio stars (Yusef-Zadeh *et al.* 2014a) assuming the standard model for a spherically-symmetric, homogeneous wind of fully ionized gas (Panagia & Felli 1975). The mass-loss rates obtained using the radio and NIR techniques agree within a factor of two. However, the mass-loss rate from IRS 33E was estimated to have only one-third of that derived from model atmosphere calculations given by Martins *et al.* (2007).

Residual instrumental distortions, as well as a number of other uncertainties, in the mosaiced results of NIR adaptive optics observations can be significant within  $10''$  of Sgr A\* (Fritz *et al.* 2010; Yelda *et al.* 2010). The detection of young stars at radio wavelengths, however, provides a means of registering the Galactic center radio and NIR frames to few milliarcsecond (mas) precision with respect to the position of Sgr A\*. Radio counterparts of eight NIR stars within  $\sim 10''$  of Sgr A\* have been identified. The nearest detected radio star, IRS 16NE, is only  $1.1''$  away from Sgr A\*. Radio emission arises from the ionized winds close to the photospheres of massive stars, whereas SiO masers arise from inside the dust formation zone of AGB stars. Localizing the radio emission from massive stars could therefore yield more accurate stellar positions than the techniques that rely on SiO masers as a reference. Thus, accurate astrometry and proper motion of sources near Sgr A\* can be achieved by registering radio and NIR frames. Accurate estimates of the stellar velocity near Sgr A\* should have implications on whether any of the disk stars are unbound (see Reid *et al.* 2007) or place a limit on the unseen mass of stars near Sgr A\*.

Proper motions of massive stars orbiting Sgr A\* can also be detected in the radio. Although relative proper motions can be accurately determined in NIR images, the first of such measurements assumed an isotropic evolved stellar cluster, having zero mean motion with respect to Sgr A\*, thus removing the average motion of the stars. At radio wavelengths, the determination of the proper motions of massive stars is similar to SiO maser-based measurements and can be determined without making any assumptions about the spatial distribution of the cluster. More recently, Yelda *et al.* (2010) and Gillessen *et al.* (2009) have used the radio astrometric system from the masers and do not use the assumption of zero rotation mean motion. The advantage of using young, massive stars over SiO sources is that radio stars are members of the young stellar cluster and lie within a few arcseconds of Sgr A\*, whereas SiO masers are more than  $7''$  away. Another advantage of measuring proper motions in radio is that source confusion is far lower than in the NIR, reducing the possibility of determining the positions of misidentified stars.

Here we present the results of our recent sensitive measurements within the inner  $30''$  of Sgr A\*. First, in §3.1, we report the first proper motion measurements of eight young stars determined using two epochs of radio observations separated by  $\sim 31$  months. These eight stars were detected in two epochs: 5 August 2011 (2011.59) and 21 February 2014 (2014.14). Because there were no NIR observations at the same epochs as the radio observations, we predicted the positions of NIR-identified stars at the 2014.14 epoch and compared them to

the radio positions. The predicted NIR positions were calculated using the proper motion measurements of Lu *et al.* (2009) and Paumard *et al.* (2006). Second, in §3.2 we present updated mass-loss rates of massive stars from ionized stellar winds at 34 and 44 GHz and compare them with the determination of mass loss rates from NIR observations. Third, in §3.3 we give new and updated positions of radio stars near the Galactic center. The list of 318 compact radio sources in Sgr A West includes the magnetar SGR 1745-29, detected at 34 GHz, and the identities of NIR stellar counterparts to 45 of the sources.

## 2. Observations and Data Reduction

### 2.1. Radio Data

We obtained two sets of A-array observations with the Karl G. Jansky Very Large Array (VLA). The first set of observations of the stellar cluster at the Galactic center were obtained on July 8–9, 2011 and August 31–September 1, 2011 at 44 GHz (program 11A-224). The two pairs of A-array observations provided data for construction of an image of the  $30''$  region surrounding Sgr A\* with a resolution of  $\sim 82 \times 42$  mas. Further details of these first-epoch observations are given in Yusef-Zadeh *et al.* (2014a). This yields a first epoch observation with an effective date of 5 August 2011.

We reobserved the region within  $30''$  of Sgr A\* on 2014 February 21, again using the VLA in its A-configuration at 44 GHz. The Q-band (7mm band) was used in the 3-bit system, which provided full polarization correlations in 4 basebands, each 2 GHz wide, centered at 41.6, 43.6, 45.6 and 47.6 GHz, respectively. Each baseband was composed of 16 subbands, each 128 MHz wide. Each subband was made up of 64 channels and channels were 2 MHz wide. These two epochs of 44 GHz observations, with effective bandwidths of  $2 \times 128$  MHz and 8 GHz, were used to measure proper motions.

We also carried out A-array observations (program 14A-232) in the Ka (9mm) band on March 9, 2014 at 34.5 GHz. We used the 3-bit system, which provided full polarization in 4 basebands, each 2 GHz wide. Each subband was made up of 64 channels and channels were 2 MHz wide. We used the same calibration strategy as we did for the Q-band observations. In all our observations, we used 3C286 to calibrate the flux density scale and used 3C286 and J1733-1304 (aka NRAO530) to calibrate the bandpass. We used J1744-3116 to calibrate the complex gains. A Phase and amplitude self-calibration procedure was applied to all data using the bright radio source Sgr A\*. We used OBIT (Cotton 2008) to construct radio images. The positions of radio sources are determined with respect to the absolute position of Sgr A\*. Sgr A\* provides a great astrometric reference, especially at high resolutions where there is very good contrast with diffuse emission associated with orbiting ionized gas. The absolute position and the proper motion of Sgr A\* are known at a level of 10 mas (Yusef-Zadeh, Choate & Cotton 1999; Reid *et al.* 2003) and  $\sim 1$  mas yr $^{-1}$  (Reid *et al.* 2003). This source is used as the astrometric reference as it cancels many of the systematic errors arising from the use of external calibrators.

## 2.2. Near-IR Data

We searched for NIR counterparts to compact radio sources using high-angular resolution adaptive optics (AO) assisted imaging observations acquired with the VLT/NACO <sup>1</sup>. A  $K_s$ -band (central wavelength  $2.18\ \mu\text{m}$ ) image was obtained in a rectangular dither pattern on 12 September 2012, using the S27 camera with a pixel scale of  $\sim 0.027''\ \text{pixel}^{-1}$  and locking the AO on the supergiant IRS 7, located about  $5.5''$  north of Sgr A\*.  $L'$ -band observations were obtained during various observing runs between June 2012 and September 2012. The  $L'$  data were acquired in speckle mode, i.e. with the AO system switched off. Details of the observations are given in Table 1. In  $L'$  we observed five fields with different pointing and depths. Field 1 was centered on Sgr A\*, and Fields 2–5 were offset by approximately  $20''$  to the northeast, southeast, southwest, and northwest, respectively.

Standard NIR image data reduction was applied as a first step: flat-field correction, sky subtraction, and interpolation of bad pixels. Finally, the images of individual pointings were combined into large mosaics. In the case of the  $L'$  image, the speckle holography technique, as described in Schödel et al. (2013), was applied to the thousands of speckle frames across the FOV to create final high-Strehl images for each pointing. The number of frames varies across FOV and is given by  $N \times \text{NDIT}$  in Table 1: 34000 in field 1 and 12750 in Field 4. The Strehl value is estimated  $\sim 60\%$ . The images of each pointing were then combined into a large mosaic. Pupil tracking was used during the observations to improve the subtraction of the high and rapidly varying background in  $L'$ . Therefore the field-of-view (FOV) changed continuously and the individual exposures had to be de-rotated. The changing FOV resulted in a slightly smaller effective area of the mosaic.

We used the PSF fitting package *StarFinder* (Diolaiti et al. 2000) to detect stars and measure their pixel positions and flux. Photometric calibration in  $K_s$  was done with the star IRS 16C (Rafelski et al. 2007, Schödel 2010). From comparison with ESO zero points taken during routine quality control within a month of the observations we estimate a systematic uncertainty of our calibration of  $1\sigma < 0.05\ \text{mag}$ . Photometric calibration in  $L'$  was done with the stars IRS 16C and IRS 16 NW (Schödel et al. 2010). Comparison with ESO zero points from June to September of the same year lead us to estimate a  $1\sigma$  systematic uncertainty of about  $0.1\ \text{mag}$ . Because of the large field-of-view we extracted PSFs locally, for small overlapping fields, very similar to the procedure described in Schödel (2010). From the difference of stellar fluxes measured with different PSFs in overlapping sub-fields we estimated the systematic uncertainty of the photometry due to limitations of our knowledge of the PSF. This uncertainty was estimated to be  $0.05\ \text{mag}$  for both  $K_s$  and  $L'$  and was added in quadrature to the formal uncertainties computed by *StarFinder*. Finally, we calibrated the images astrometrically by using the positions and proper motions of SiO maser stars in the Galactic center (Reid et al. 2007). We used the positions and proper motions of the SiO masers IRS9, IRS7, IRS12N, IRS28, SiO-15, IRS10EE, IRS15NE, IRS17, IRS19NW as published by (Reid et al. 2007) to calculate their position for the epoch of the images. The masers' pixel positions in

---

<sup>1</sup>Based on observations made with ESO Telescopes at the La Silla or Paranal Observatories under programs ID 089.B-0503

the NIR images were measured via PSF fitting with StarFinder. Finally, the astrometry was solved with the IDL solve-astro routine from ASTROLIB. NO distortion solution was fitted, just linear terms. Note that we did not correct for any camera distortions. In order to check the astrometric accuracy we performed 100 runs of a Monte Carlo simulation. The maser positions were varied randomly within their uncertainties (combined radio + NIR), using a normal distribution with a standard deviation corresponding to the radio/NIR uncertainties. Each time the astrometry was solved and the NIR maser positions were compared to their radio positions. From these simulations we obtained a standard deviation for the position of each maser star. Additionally, we performed a jackknife test by using only 8 out of 9 maser stars. The standard deviations between the (astrometric) NIR position and the prediction from the radio measurements were very similar to the Monte Carlo test. From Monte Carlo simulations (varying the positions of the masers within their NIR and radio uncertainties), we estimated that the astrometric precision was better than one pixel (27 mas) across the region of the  $K_s$  and  $L'$  mosaics where the radio sources are located.

### 3. Results

#### 3.1. Proper Motion Measurements

We used two techniques to compare radio and NIR proper motion measurements. First, we measured the proper motions of the radio stars using data taken in 2011.59 (first epoch) and 2014.14 (second epoch). These estimates are made only from radio observations. We then compare these radio-derived proper motion values with those exclusively from NIR observations. A second technique involves the prediction of the NIR stellar source positions at the 2014.14 epoch and then comparing those predicted positions with the 2014.14 radio positions. The reason for doing this second type of comparison is because we don't have simultaneous radio and NIR observations.

##### 3.1.1. Proper Motions of Radio Stars

In our first and second epoch radio observations on 2011.59 and 2014.14, the well-known young, massive stars in the central Sgr A\* cluster (e.g., IRS 16C, IRS 16NE, IRS 16SE2, IRS 16NW, IRS 16SW, AF, AFNW, IRS 34W and IRS 33E), as well as the heavily extincted NIR source IRS 5, were detected with rms noise  $\sigma \sim 61$  (S/N  $\sim 4$ -20) and  $\sim 22 \mu\text{Jy}$  (S/N  $\sim 4$ -31), respectively. These radio stars are isolated from the mini-spiral HII region and appear to be unresolved in two-dimensional Gaussian fits. Our analysis of the proper motion between August 2011 and February 2014 indicates uncertainties that are dominated by the poor sensitivity of our 2011 data, which suffered from relatively narrow bandwidths ( $2 \times 128$  MHz). We measure proper motions of these eight stars with respect to Sgr A\*. Columns 1 to 5 in Table 2 show the list of sources, the proper motion  $\mu_x$  and  $\mu_y$  in RA and Dec, and the corresponding tangential velocity in RA and Dec, respectively. A proper motion of  $1 \text{ mas yr}^{-1}$  corresponds to  $\sim 40 \text{ km s}^{-1}$  at the Galactic center distance of 8 kpc. As a reference,

we also include in Table 2 the parameters of the fit to Sgr A\* (Reid and Brunthaler 2004). The assumed proper motion of Sgr A\* is  $6.379 \pm 0.024$  mas yr<sup>-1</sup>. This motion is due to the orbit of the Sun around the center of the Galaxy (Reid and Brunthaler 2004). The residual error left after removing the solar motion is  $-0.4 \pm 0.9$  km s<sup>-1</sup> running perpendicular to the plane of the Galaxy. IRS 16C lies closest to Sgr A\* in our sample and gives the highest proper motion values of  $-11.82$  and  $9.8 \pm 1.61$  mas yr<sup>-1</sup>, in RA and Dec, respectively. We now compare these proper motion measurements with those determined from NIR data.

The orbits of young stars in the stellar disk are determined in the NIR observations. This is generally done by measuring the proper motion of several hundred stars distributed around Sgr A\*. In this technique the zero point of the motion of the stellar cluster is determined by assuming isotropy. Unlike the NIR proper motion measurements, radio proper motion measurements (Reid *et al.* 2007), using either SiO masers or young radio stars, are carried out in the frame tied to Sgr A\*, known to be stationary and requires no isotropy assumption. To compare our radio-derived proper motion values with those from NIR measurements, we list published measurements from Lu *et al.* (2009) and Paumard *et al.* (2006) in Table 2. The radio and NIR data generally agree within  $1\sigma$ . The sources IRS 16C, AFNW, and AF, however, show discrepancies between the two sets of measurements. IRS 16C, which is offset from Sgr A\* by  $\sim 1.17''$ , is one of the brightest Galactic center massive stars in the central cluster, has a spectral type of Ofpe/WN9 (Martin *et al.* 2007), and significant tangential acceleration (Lu *et al.* 2009). The proper motion of IRS 16C deviates by  $\sim 3.3\sigma$  and  $\sim 1.2\sigma$  in RA and Dec when compared to NIR measurements given by Lu *et al.* (2009) and Paumard *et al.* (2006). The proper motions of IRS 16SE2, AFNW, and AF differ by  $\sim 3.7\sigma$  in RA,  $\sim 2.3\sigma$  in RA,  $\sim 5.2\sigma$  in Dec from those of Paumard *et al.* (2006). The AFNW and AF stars (Paumard *et al.* 2006) are isolated stars displaced from Sgr A\* by  $\sim 8.44''$  and  $9.47''$  (sources 110 and 126 in Table 6), respectively. Although background subtraction is applied in our fitting procedures, these radio stars are located in a region where there is very little nebular emission, so their flux and position measurements do not need background subtraction and are more accurate because they are not contaminated by confusing ionized features. The origin of these discrepancies is unknown, but it is possible that it is due to the curvature of the orbit that has not been accounted for in the IRS 16C proper motion measurements. Alternatively, it is possible that radio emission from these stars arises not only from the ionized winds of mass-losing stars, but also from the bow shock due to the motion of the star with respect to the ISM near Sgr A\*. The data presented here are limited by the small sample of sources and high positional errors in our first epoch measurements. In spite of these limitations, the radio and NIR proper motion measurements give consistent values for most of the stellar sources that we studied. Future radio observations with similar sensitivity and resolution to those of our second epoch observation should reduce the uncertainties in radio-derived proper motions.

### 3.1.2. The Positions of Radio and NIR-identified Stars

Because we did not have simultaneous observations of the stellar cluster at radio and NIR wavelengths, we were not able to carry out direct astrometric comparisons, as was done in Yusef-Zadeh *et al.* (2014a). We therefore used a different approach for the comparison of the positions of radio and NIR stars.

Using the catalogs of proper motion data given by Paumard *et al.* (2006) and Lu *et al.* (2009) we first computed the predicted X/Y offsets of NIR stars relative to Sgr A\*, by evolving the orbits of the stars to the 2014.14 epoch of radio observations. The 2014.14 positions were computed for a total of 31 and 90 stars from each of the above catalogs, respectively. These Right Ascension (RA) and Declination (Dec) offsets from Sgr A\* were then translated into absolute RA/Dec by assuming that the RA/Dec (J2000) of Sgr A\* is  $17^h45^m40^s.0383, -29^\circ00'28''.069$ .

The absolute coordinates of the orbit-evolved NIR sources were translated into the frame of our 2014.14 radio image and sources common to both the NIR and radio catalogs were found using the IRAF task “xyxymatch.” We then determined a transformation between the radio and IR frames using the IRAF task “geomap”, which computes changes in scale factor and rotation between the coordinate systems of the two frames, in order to remove any overall differences between the radio and NIR frames due to instrumentation. This computation also gives us rms residual offsets between the two frames for the list of common sources.

A total of 6 radio stars in the 2014.14 radio image were found to have NIR counterparts in the catalog of objects from Lu *et al.* (2009). The six identified sources are IRS 16C, IRS 16NE, IRS 16NW, S3-5, IRS 16SW and IRS 33E. Columns 1 to 7 of Table 3 lists the names of these six stars, their predicted dX, dY offsets from Sgr A\* in arcseconds and the corresponding errors  $X_{err}$ ,  $Y_{err}$ , and the radio image pixel coordinates X(radio) and Y(radio), respectively. The predicted positions also include the acceleration term given by Lu *et al.* (2009). Sgr A\* is centered at pixel position  $3456.0 \times 3456.0$  in the 44 GHz radio image and the pixel size is 8.68159 mas. The transformation of the two sets of coordinates between the radio and NIR images resulted in a small overall shift of  $\sim 6$  and  $\sim 8$  mas in the X and Y direction, respectively, which is at the level of  $1\sigma$  in the residuals of the overall transformation. There was no change in overall scale factor and no indication of rotation to a level of  $< 0.35^\circ$ . The rms residuals between the radio and NIR positions of the six sources are on the order of 0.5–0.8 pixels in the X, Y directions, which is equivalent to 5–7 mas in the radio image.

There were 21 NIR stellar sources from the catalog of Paumard *et al.* (2006) that had radio counterparts. We measured the corresponding pixel locations in the 44 GHz radio image for all of the NIR stars, which resulted in overall X and Y shifts between the two frames of 5 and 1 mas, respectively, and again no indication of any significant change in either pixel scale or rotation. Columns 1 to 10 of Table 4 shows the ID numbers and names of stars that Paumard *et al.* (2006) used, RA, Dec, the predicted offset positions from Sgr A\*, the predicted NIR and radio pixel positions in RA and Dec directions, respectively. The residuals in the positions of the 21 sources between the radio and NIR frames are roughly 2.1 – 2.6 pixels, equivalent to  $\sim 18$  to 22 mas in X and Y directions, respectively. The higher



residuals in this set of measurements is mainly due to fairly large uncertainties in the proper motions that were used to extrapolate the positions of the NIR stars to the 2014.14 epoch of the radio data. Paumard *et al.* (2006) do not quote uncertainties in the original positions of the NIR stars, so we assumed a typical uncertainty of  $\sim 5$  mas based on nature of their data. The average uncertainty in the proper motions leads to an additional scatter in the extrapolated 2014 positions of  $\sim 10$  mas in each axis. When combined with the uncertainty of the original positions, this accounts for most of the  $\sim 20$  mas residuals in the positions of individual stars between the radio and NIR frames.

### 3.2. Ionized Stellar Winds

The radio stars that we detected at 44 GHz (Yusef-Zadeh *et al.* 2014a) coincide with luminous NIR sources having P-Cygni profiles, which is strong evidence for stellar winds (Najarro *et al.* 1997; Martins *et al.* 2007). The radio emission most likely arises from the ionized winds of the hot stars (Panagia & Felli 1975). We previously determined the mass-loss rates of individual radio stars from their 44 GHz emission (Yusef-Zadeh *et al.* 2014a) using the standard model for a spherically-symmetric, homogeneous wind of fully ionized gas expanding with a constant terminal velocity (Panagia & Felli 1975; Contreras *et al.* 1996). Given the improved signal-to-noise ratio of the radio data that is presented here, we update the mass loss rates of nine well known stellar sources at 34.5 and 44.6 GHz. To estimate the mass loss rate, we use the expression by Panagia and Felli (1975) given below,

$$\dot{M} = 2.938 \times 10^{-6} S_{\nu}^{0.75} \nu^{-0.6} T_e^{-0.075} \mu v_{wind} d^{1.5} / Z^{0.5} M_{\odot} \text{yr}^{-1},$$

where the flux density  $S_{\nu}$  is in mJy, electron temperature  $T_e$  in  $10^4\text{K}$ , the mean molecular weight  $\mu$  is 1.2, the terminal wind velocity  $v_{wind}$  in units of  $10^3 \text{ km s}^{-1}$  the distance  $d$  in 1 kpc and the solar metallicity  $Z=1$ . For  $S_{\nu} = 1$  mJy,  $d=8$  kpc, and the above parameters, stellar mass loss rates are  $\dot{M} = 3.81 \times 10^{-5}$  and  $3.39 \times 10^{-5} M_{\odot} \text{yr}^{-1}$  at  $\nu = 34.5$  and 44.6 GHz, respectively.

Table 5 compares the mass-loss rates determined from the radio measurements at 34.5 GHz (8.695 mm) and 44.6 GHz (6.723 mm) with the NIR mass-loss rate estimates from model atmosphere calculations (Martins *et al.* 2007). Columns 1 to 12 of Table 5 show the NIR identified stellar sources, the terminal velocity, H to He ratio taken from Table 2 of Martins *et al.* (2007), the mean abundance, the mass loss rate from NIR model atmosphere calculations, the peak flux density at 34.5 GHz, the mass-loss rate derived from 34.5 GHz measurements, the peak flux density at 44.6 GHz and the mass-loss rate derived from 44.6 GHz measurements, respectively. The mean metallicity was estimated for each source using H and He abundances given by Martins *et al.* (2007). We include the mass-loss rate of four additional sources only at 34.5 GHz as well as IRS 16NE and IRS 16SW using radio data, even though they are binaries (Pfuhl *et al.* 2014). The model atmosphere calculations for these two binaries are not available. Table 5 adopts the Galactic center distance 7.62 kpc, as was used by Martins *et al.* (2007). A comparison between radio and NIR-determined stellar mass loss rates is shown in Figure 1. The filled red points show stellar mass loss

rates derived in the NIR and those derived from 34.5 GHz fluxes. Similarly, the unfilled blue points show the mass loss determined at 34.5 and 44.6 GHz. We note that radio-determined mass-loss rates are systematically lower than those of NIR-determined mass-loss rates. The red dashed line shows the best-fitting line assuming that the NIR-derived mass-loss rate is directly proportional to the radio-derived rate whereas the blue points show mass loss rates derived from radio flux at 44.6 GHz vs that derived at 34.5 GHz. The black dashed line indicates where the mass loss rates derived at different frequencies are equal. The offset between the red and black dashed lines shows that radio-determined mass-loss rates are on average lower than NIR-identified mass-loss rates by a factor of 2.

Radio observations provide the gross properties of the wind, whereas model atmosphere calculations require an estimate of the extinction, the detailed ionization balance of trace species, as well as the shape of the velocity profile. Thus, the mass-loss rate under the assumption of homogeneity and spherical symmetry using radio continuum data is generally simple and straight-forward to derive and perhaps more accurate (e.g., Blomme 2011). A number of recent studies indicate that there is overwhelming evidence for clumpy ionized winds from massive stars (e.g., review by Crowther 2007) and that the clumpiness factor reduces the mass-loss rate. The clumping factor  $f_{cl} = \langle \rho^2 \rangle / \langle \rho \rangle^2$  where the brackets indicate an average density over the volume in which radio continuum at all wavelengths is formed (Blomme 2011). For example, clumpiness reduces the global mass-loss rates of WR stars by roughly a factor of 3 (Crowther 2007) whereas the winds from O stars, which are highly clumpy, reduces the mass-loss rate estimate by an order of magnitude or even more (Crowther 2007; Sundqvist et al. 2011).

The mass-loss rates determined from the radio emission of Galactic center O and WR stars are systematically lower than that from NIR estimates by an average value of 2 for a total of 11 sources, as shown in Figure 1. The discrepancy in mass-loss rate estimates become more significant if the ionized winds are clumpy. We assume that the 11 sources in Table 5 represent a sample of mass-losing luminous stars in the Galactic center. Assuming WR stars only, the mass-loss rates from all stars are reduced roughly by a factor of 6. If we assume all stars are O-type, the mass-loss rate is reduced by a factor of 20. Given a mixture of WR and O stars distributed within  $10''$  of Sgr A\*, the mass-loss rate estimates from OB and WR stars are reduced by roughly an order of magnitude. Numerical simulations of wind accretion onto Sgr A\* show that the accretion rate is  $\sim 3 \times 10^{-6} M_{\odot} \text{ yr}^{-1}$  after accounting for the motion of mass-losing OB and WR stars in a disk geometry orbiting Sgr A\* (Cuadra *et al.* 2006). The reduced estimate of mass-loss rates from OB and WR stars from our radio observations implies that the accretion rate onto Sgr A\* should be roughly  $3 \times 10^{-7} M_{\odot} \text{ yr}^{-1}$ . We note that our reduced estimate of the wind accretion rate is consistent with the mass accretion estimate made from polarization measurements (Bower et al. 2003).

One of the implications of the reduced mass-loss rate of luminous young stars is the reduction in the Bondi-Hoyle accretion rate onto Sgr A\*. This is because the current paradigm assumes that Sgr A\* is fed by the partial accretion of merged stellar winds from the OB and WR stars in the inner parsec of the Galaxy (Coker & Melia 1997; Quataert 2004; Cuadra *et al.* 2006, 2008). The Bondi accretion rate onto Sgr A\* will be significantly reduced if the ionized

winds are highly clumpy, thus reducing the expected luminosity of Sgr A\* by more than an order of magnitude.

### 3.3. Compact Radio Sources at 34 GHz

One of the most interesting aspects of the new broad-band radio continuum images of the Galactic center is the detection of numerous compact radio sources, many of which appear to coincide with massive stars, photoevaporative proplyd-like objects, or evaporative gaseous globule candidates (Yusef-Zadeh *et al.* 2014a, 2015). The improved sensitivity of these new images allows for the detection of isolated weakly emitting radio sources, as well as resolving radio stars embedded within the diffuse ionized gas. Table 6 gives a list of 318 compact sources at 34.5 GHz distributed within 30'' of Sgr A\*. Entries in columns 1 to 11 in Table 6 give the source ID, NIR identified stellar source, RA and Dec, the angular distance from Sgr A\*, the positional precision, the deconvolved size, peak radio intensity, integrated intensity, and the NIR flux density at  $K_s$  and  $L'$  bands. Column 12 provides the references and comments on individual sources.

Identified NIR counterparts to the compact radio sources are listed column 2 of Table 6. Note that some of these stars may be variable, but we did not investigate this here. Sources detected in both  $K_s$  and  $L'$  can be considered high confidence detections. Also, the sources detected only at  $K_s$  appeared to be clearly point-like, although surprisingly faint. It is not clear why they appear so faint, perhaps because of differential extinction across the Galactic center, thus reducing the flux. Alternatively, they could be pre-main sequence stars photoionized externally by the strong radiation field (Yusef-Zadeh *et al.* 2015). We identified NIR counterparts to the radio sources by simple positional matching. Sources were accepted as identical if they coincided within two NACO pixels or about 54 mas, which corresponds to the angular resolution of NACO in the  $K_s$ –band. The resolution of the radio image is  $\sim 47 \times 88$  mas. Because the radio and NIR data are not from the same epoch, the positions of the stars will not match precisely. This is why we used a relatively large tolerance for matching the positions. Nevertheless, the tolerance is sufficiently small to exclude confusion with other stars. Table 6 also shows that at least 45 of these compact radio sources have stellar counterparts in the near-IR  $K_s$  (2.18  $\mu\text{m}$ ) and  $L'$  (3.8  $\mu\text{m}$ ) bands. The number of stellar sources with radio counterparts is limited because the spatial coverage of the radio images is  $\sim 1' \times 1'$ , whereas the region covered by the five  $L'$  fields is  $\sim 50'' \times 50''$  and there are gaps between the fields.

The positions and the sizes of radio sources are determined from background-subtracted Gaussian fits to the individual radio sources. Radio sources that are unresolved are shown by dashed lines. Note the inclusion of the magnetar SGR J1745-29, ID 13 in Table 6 (Kennea *et al.* 2013; Shannon and Johnston 2013). This source was in its quiescent phase before it was identified as an X-ray outburst (Kennea *et al.* 2013). SGR J1745-29 is the closest known pulsar located 2.4'' from Sgr A\*. The detection of a compact radio source located at  $\alpha \delta (J2000) = 17^h 45^m 40^s.16795 \pm 0.00002 - 29^\circ 00' 29''.74908 \pm 0.00064$  was reported at 44.6 GHz on 2014 February 21 (Yusef-Zadeh *et al.* 2014b). Another notable collection of radio

sources coincides with IRS 21, which is comprised of six radio components, suggesting that IRS 21 is a stellar cluster similar to IRS 13N and IRS 13E.

There are several radio sources that have NIR counterparts only at  $L'$  (Table 6). Several of these sources can be found within 0.1 pc of Sgr A\*. These sources may be similar in nature to the Dusty S-cluster Object DSO/G2 that is currently the subject of intense observational campaigns as it passes extremely close to the central black hole (Gillessen et al. 2012; Witzel et al. 2014; Pfuhl et al. 2015; Valencia-Schneider et al. 2015). Alternatively, recent radio study of  $L'$  sources with radio counterparts argues that they are massive young stellar objects (YSOs). In this interpretation, thermal radio emission from the ionized gas of the  $L'$  sources is being photo-evaporated from the disks of YSOs by the UV radiation from hot stellar sources in the Galactic center (Yusef-Zadeh et al. 2014a).

Figure 2 shows a 34.5 GHz image of Sgr A West. A close-up view of this image includes circles and ID numbers, from column 1 of Table 6, identifying compact radio sources. Figure 3 shows a  $3.8\mu\text{m}$  image of the region within  $\sim 20''$  of Sgr A\*. Labels show the NIR-identified stellar sources that have radio counterparts, as listed in column 2 of Table 6. The insets show close-up views of the crowded regions of Sgr A West where the stellar clusters IRS 16 and IRS 13 lie. Figures 4a,b show large and scaled-up views of the central region of Sgr A West at 34.5 GHz, respectively. Labels indicate radio stars with NIR stellar counterparts, as shown in Figure 3.

#### 4. Conclusions

With the improved sensitivity of recent VLA radio observations of the Galactic center, we provided three aspects of the radio properties of objects within  $30''$  of Sgr A\* as discussed below.

First, we calculated the proper motion of radio stars orbiting Sgr A\*. Our proper motion measurements illustrate that future high resolution radio observations at multiple epochs can compete with other methods of determining the orbit of stars, as done at NIR wavelengths. One main advantage that radio studies provide is that the positions of stars are measured directly and accurately with respect to Sgr A\*, a feat that is not possible with NIR imaging. This is because of the lack of a steady component of NIR emission from Sgr A\* which anchors the radio frame. Another advantage is that source confusion is far lower in the radio than in the NIR, thus, one can avoid biased positions of the young stars at NIR. Lastly, the relative motion between the cluster and Sgr A\* which has already been tested for SiO masers (Reid et al. 2007), but the greater number of radio stars may provide useful constraints.

Second, we estimated the mass-loss rates of massive stars near Sgr A\* using radio data and compared these values with those estimated from model atmosphere calculations. Assuming that the winds are clumpy, the discrepancy between radio and NIR mass-loss estimates would reduce the near-IR-determined mass loss rate of WR and O stars by factors ranging between 6 and 20, respectively. This implies a downward revision of the mass accretion rate by an order of magnitude to  $\sim 3 \times 10^{-7} M_{\odot} \text{ yr}^{-1}$  if the merging of ionized winds from massive

stars is responsible for the accretion onto Sgr A\* (Cuadra *et al.* 2006).

Third, we reported the detection of 318 radio sources within the inner 30'' of Sgr A\*. The comparison of radio and NIR data indicated that at least 45 of the radio sources are stars and have counterparts at both  $K_s$  and  $L'$  bands. The radio sources include compact HII regions, proplyd-like objects, externally heated massive YSOs, ionized winds from massive stars as well as nonthermal sources. Future studies of the spectra of these sources will be useful in identifying the true nature of radio sources within 30'' of Sgr A\*. In addition, the future VLTI instrument GRAVITY can provide astrometry with a precision up to 10 microarcseconds, but only relative to a reference star within 2'' of the target. To measure orbits of stars around Sgr A\*, it is still necessary to tie them into the large astrometric reference frame. The detection of radio stars opens a new window for astrometric calibration. There are several radio stars within 2'' of Sgr A\* so that can be used for calibration and for testing the accuracy of the calibration. Even if only a single reference star is used for GRAVITY (IRS 16C or IRS 16NW), then one can still compare the two calibration methods: (a) the traditional NIR-maser proper motion calibration and (b) a more direct calibration via radio detection and proper motions.

Acknowledgments: This work is partially supported by the grant AST-0807400 from the NSF and the European Research Council under the European Union’s Seventh Framework Program (FP/2007-2013). The National Radio Astronomy Observatory is a facility of the National Science Foundation, operated under a cooperative agreement by Associated Universities, Inc.

## REFERENCES

- Blomme, R. 2011, Bulletin de la Societe Royale des Sciences de Liege, 80, 67
- Bower, G. C., Wright, M. C. H., Falcke, H., & Backer, D. C. 2003, ApJ, 588, 331
- Coker, R. F., & Melia, F. 1997, ApJ, 488, L149
- Contreras, M. E., Rodriguez, L. F., Gomez, Y., & Velazquez, A. 1996, Radio Emission from the Stars and the Sun, 93, 29
- Cotton, W. D. 2008, PASP, 120, 439
- Crowther, P. A. 2007, ARA&A, 45, 177
- Cuadra, J., Nayakshin, S. & Martins, F. 2008, MNRAS, 383, 458
- Cuadra, J., Nayakshin, S., Springel, V., & Di Matteo, T. 2006, MNRAS, 366, 358
- Diolaiti, E., Bendinelli, O., Bonaccini, D., et al. 2000, A&AS, 147, 335
- Fritz, T. K., Chatzopoulos, S., Gerhard, O., et al. 2014, arXiv:1406.7568
- Fritz, T. K., Gillessen, S., Dodds-Eden, K., et al. 2010, ApJ, 721, 395

- Ghez, A. M., Hornstein, S. D., Lu, J. R., et al. 2005, *ApJ*, 635, 1087
- Gillessen, S., Eisenhauer, F., Fritz, T. K., et al. 2009, *ApJ*, 707, L114
- Gillessen, S., Genzel, R., Fritz, T. K., et al. 2012, *Nature*, 481, 51
- Kennea, J.A., Burrows, D.N., Kouveliotou, C., Palmer, D.M., et al. 2013, *ApJ*, 770, L24
- Lu, J. R., Ghez, A. M., Hornstein, S. D., et al. 2009, *ApJ*, 690, 1463
- Martins, F., Genzel, R., Hillier, D. J., et al. 2007, *A&A*, 468, 233
- Menten, K. M., Reid, M. J., Eckart, A., & Genzel, R. 1997, *ApJ*, 475, L111
- Moultaka, J., Eckart, A., & Schödel, R. 2009, *ApJ*, 703, 1635
- Najarro, F., Krabbe, A., Genzel, R., et al. 1997, *A&A*, 325, 700
- Panagia, N., & Felli, M. 1975, *A&A*, 39, 1
- Paumard, T., Genzel, R., Martins, F., Nayakshin, S., Beloborodov *et al.* 2006, *ApJ*, 643, 1011
- Pfuhl, O., Alexander, T., Gillessen, S., et al. 2014, *ApJ*, 782, 101
- Pfuhl, O., Gillessen, S., Eisenhauer, F., et al. 2015, *ApJ*, 798, 111
- Quataert, E. 2004, *ApJ*, 613, 322
- Rafelski, M., Ghez, A. M., Hornstein, S. D., Lu, J. R., & Morris, M. 2007, *ApJ*, 659, 1241
- Reid, M. J., & Brunthaler, A. 2004, *ApJ*, 616, 872
- Reid, M. J., Menten, K. M., Genzel, R., et al. 2003, *ApJ*, 587, 208
- Reid, M. J., Menten, K. M., Trippe, S., Ott, T., & Genzel, R. 2007, *ApJ*, 659, 378
- Rubilar, G. F., & Eckart, A. 2001, *A&A*, 374, 95
- Schödel, R. 2010, *A&A*, 509, AA58
- Schödel, R., Feldmeier, A., Kunneriath, D., et al. 2014, *A&A*, 566, AA47
- Schödel, R., Yelda, S., Ghez, A., et al. 2013, *MNRAS*, 429, 1367
- Schödel, R., Najarro, F., Muzic, K., & Eckart, A. 2010, *A&A*, 511, AA18
- Shannon, R. M., & Johnston, S. 2013, *MNRAS*, 435, L29
- Sundqvist, J. O., Puls, J., Feldmeier & Owocki, S. P. 2011, *A&A*, 528, 64
- Valencia-Schneider et al. 2015, *ApJ*, 800, 125
- Viehmann, T., Eckart, A., Schödel, R., et al. 2005, *A&A*, 433, 117

- Witzel, G., Ghez, A. M., Morris, M. R., et al. 2014, *ApJ*, 796, LL8
- Yelda, S., Ghez, A. M., Lu, J. R., et al. 2014, *ApJ*, 783, 131
- Yelda, S., Lu, J. R., Ghez, A. M., et al. 2010, *ApJ*, 725, 331
- Yusef-Zadeh, F., Choate, D., & Cotton, W. 1999, *ApJ*, 518, L33
- Yusef-Zadeh, F., Roberts, D. A., Bushouse, H., et al. 2014a, *ApJ*, 792, LL1
- Yusef-Zadeh, F., Roberts, D., Heinke, C., et al. 2014b, *The Astronomer’s Telegram*, 6041, 1
- Yusef-Zadeh, F., Roberts, D. A., Wardle, M., et al. 2015, *ApJ*, 801, LL26

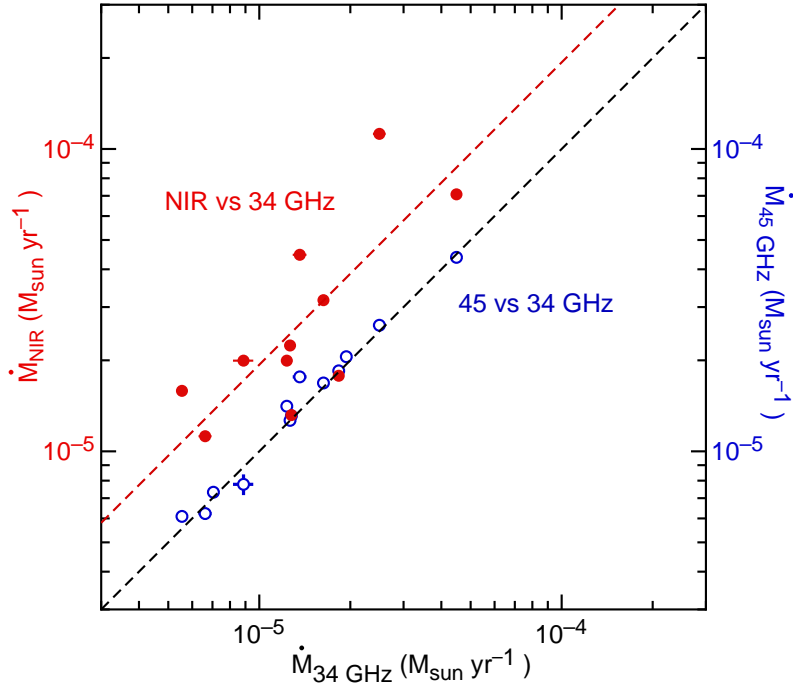


Fig. 1.— Comparison of stellar mass loss rates derived in the NIR with those derived from 34.5 GHz fluxes shown in red. Red dashed line shows the best-fitting line to the red points (see text). Blue points show mass loss rate derived from radio flux at 44.6 GHz flux vs that derived at 34.5 GHz. The black dashed line indicates where the mass loss rates derived at different frequencies are equal.



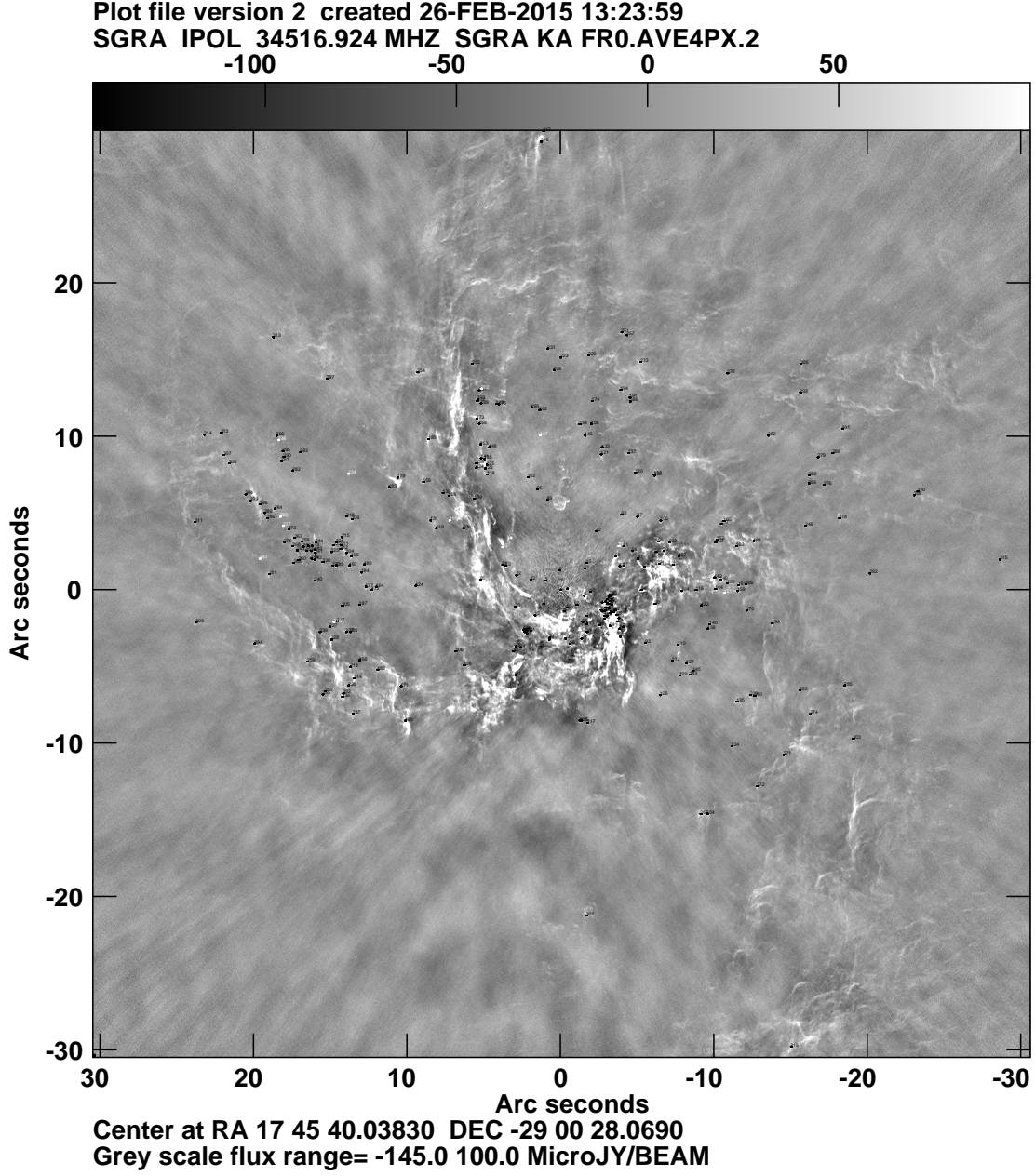


Fig. 2.— A 34.5 GHz image of Sgr A West with the spatial resolution of  $886 \times 465$  mas with  $PA = -1.6^\circ$ . Every 4 pixels is displayed because of the large size of the image. Filled circles coincide with the positions of 318 sources given in Table 6. The labels can be viewed when the image is enlarged. (High resolution images in this paper are available by request).

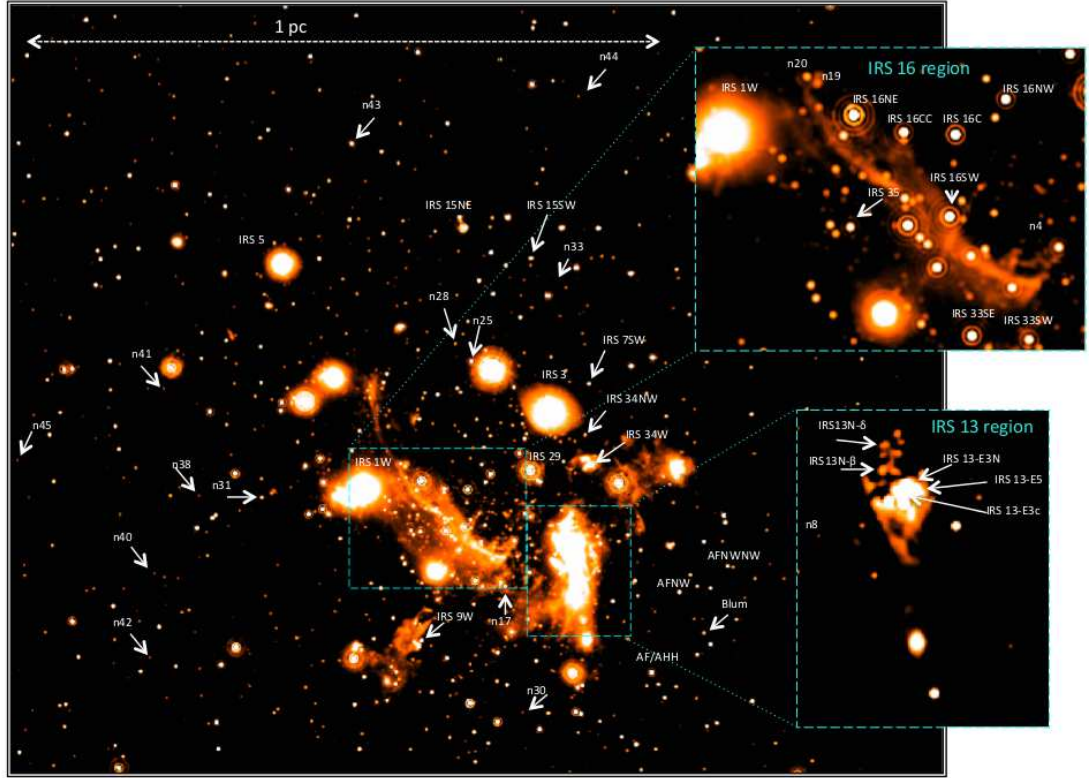


Fig. 3.— A  $3.8\mu\text{m}$  image within  $20'' \times 20''$  of Sgr A\*. Labels show NIR sources with radio counterparts with positions given in Table 6. Insets show close-up views of two stellar clusters IRS 16 and IRS 13.

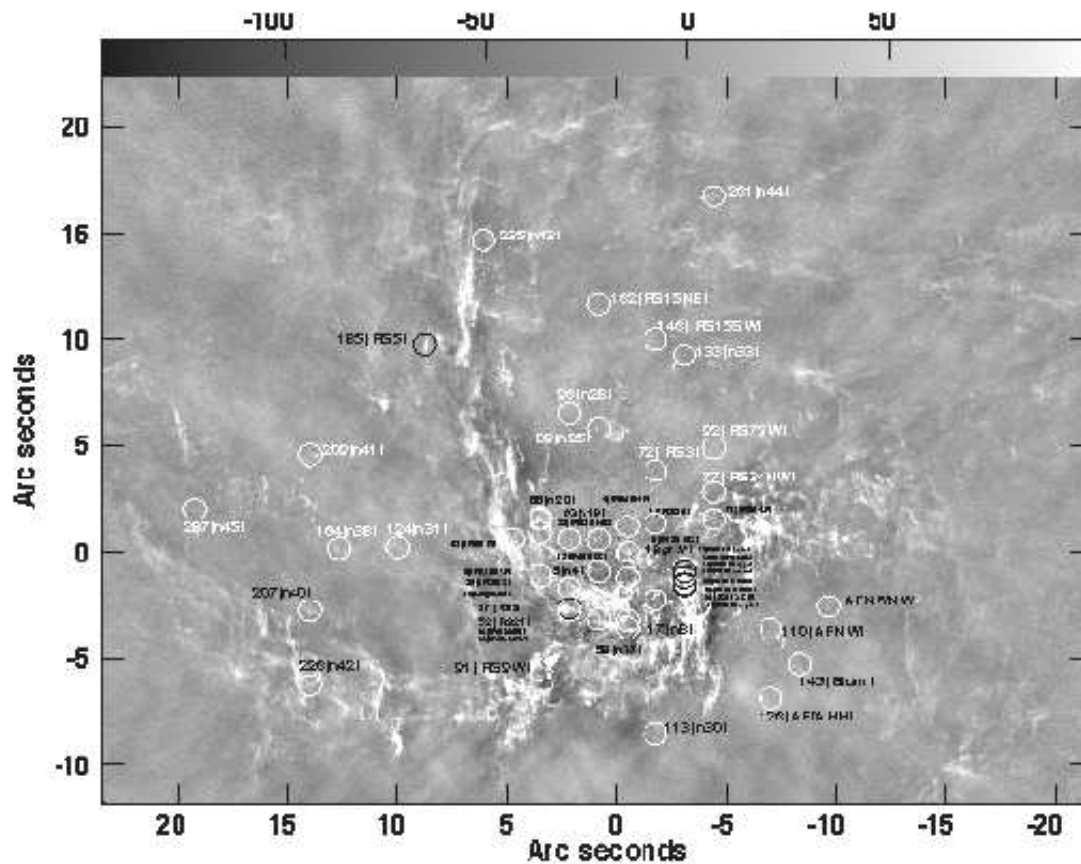


Fig. 4.— (a) Similar to Figure 1 except that the central  $\sim 40'' \times 30''$  of Sgr A West is shown. Circles and labels point to the positions of radio sources with NIR counterparts. (b) Similar to (a) except that the central  $\sim 5'' \times 7''$  is displayed. Small labels are visible if zoomed in (as in Fig. 2).

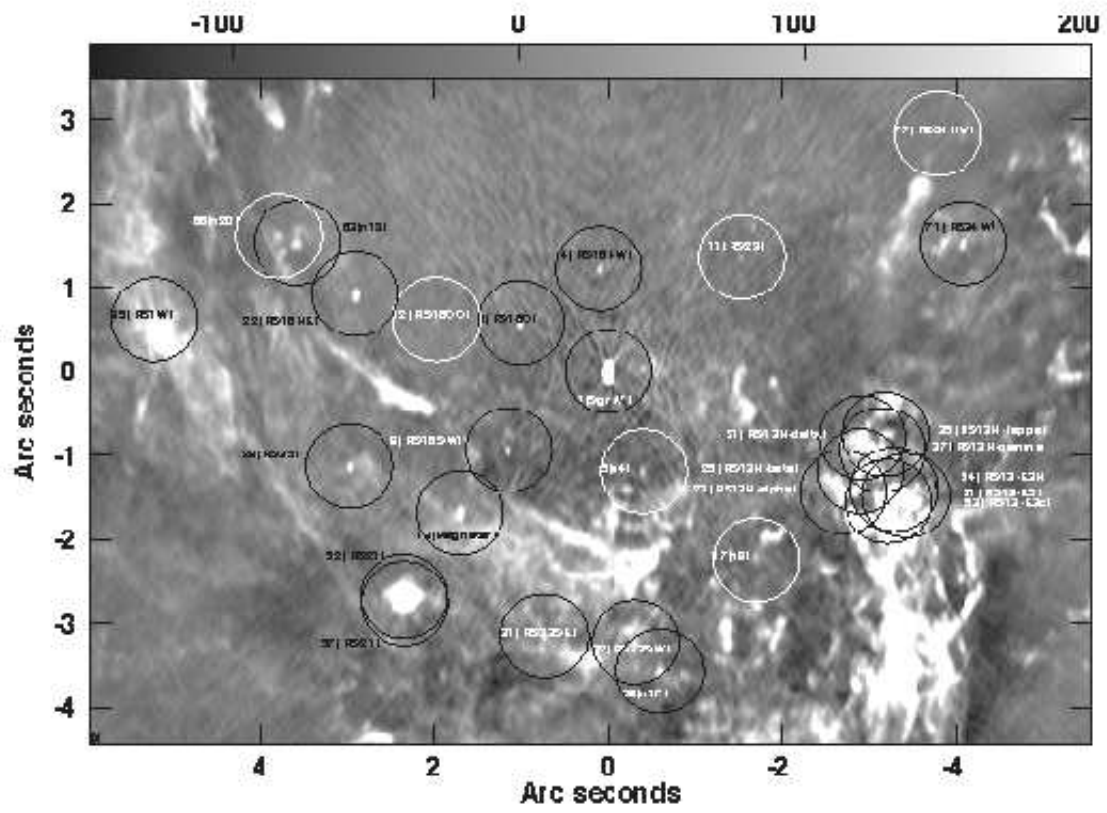


Table 1: Details of IR Observations

Date	$\lambda_{\text{central}}$ [ $\mu\text{m}$ ]	$\Delta\lambda$ [ $\mu\text{m}$ ]	N <sup>a</sup>	NDIT <sup>b</sup>	DIT <sup>c</sup> [s]
12 Sept 2012	2.18	0.35	32	60	1
<i>L'</i> Field 1					
27 June 2012	3.80	0.62	102	125	0.25
14 July 2012	3.80	0.62	68	125	0.25
20 July 2012	3.80	0.62	34	125	0.25
12 Aug 2012	3.80	0.62	34	125	0.25
14 Aug 2012	3.80	0.62	34	125	0.25
<i>L'</i> Field 2					
17 July 2012	3.80	0.62	34	125	0.25
20 July 2012	3.80	0.62	34	125	0.25
12 Aug 2012	3.80	0.62	34	125	0.25
14 Aug 2012	3.80	0.62	34	125	0.25
<i>L'</i> Field 3					
17 July 2012	3.80	0.62	34	125	0.25
20 July 2012	3.80	0.62	34	125	0.25
12 Aug 2012	3.80	0.62	34	125	0.25
26 Aug 2012	3.80	0.62	34	125	0.25
6 Sep 2012	3.80	0.62	34	125	0.25
<i>L'</i> Field 4					
17 July 2012	3.80	0.62	34	125	0.25
20 July 2012	3.80	0.62	34	125	0.25
13 Aug 2012	3.80	0.62	34	125	0.25
<i>L'</i> Field 5					
17 July 2012	3.80	0.62	34	125	0.25
2 Aug 2012	3.80	0.62	34	125	0.25
13 Aug 2012	3.80	0.62	68	125	0.25
21 Aug 2012	3.80	0.62	34	125	0.25
26 Aug 2012	3.80	0.62	34	125	0.25

<sup>a</sup> Number of (dithered) exposures<sup>b</sup> Number of integrations that were averaged on-line by the read-out electronics<sup>c</sup> Detector integration time. The total integration time of each observation amounts to  $N \times \text{NDIT} \times \text{DIT}$

Table 2. Proper motion of radio stars: Epoch1=2011.59, Epoch2=2014.14

Source	Proper Motion RA ( $mas\ yr^{-1}$ )	Proper Motion Dec ( $mas\ yr^{-1}$ )	Proper Motion RA ( $km\ s^{-1}$ )	Proper Motion Dec ( $km\ s^{-1}$ )
IRS 16NE (7mm)	$2.78 \pm 0.47$	$-11.18 \pm 0.82$	$111.2 \pm 18.8$	$-447.4 \pm 32.9$
IRS 16NE (IR-Lu)	$3.11 \pm 0.06$	$-10.94 \pm 0.06$	—	—
IRS 16NE (IR-Paumard)	—	—	$104 \pm 49$	$-379 \pm 47$
IRS 16C (7mm)	$-12.03 \pm 0.99$	$9.64 \pm 1.65$	$-481.2 \pm 39.5$	$385.7 \pm 65.9$
IRS 16C (IR-Lu)	$-8.74 \pm 0.05$	$7.42 \pm 0.05$	—	—
IRS 16C (IR-Paumard)	—	—	$-342 \pm 50$	$302 \pm 44$
IRS 16NW (7mm)	$7.13 \pm 1.74$	$-3.46 \pm 3.12$	$285.4 \pm 69.8$	$-136.6 \pm 124.9$
IRS 16NW (IR-Lu)	$6.30 \pm 0.06$	$0.87 \pm 0.06$	—	—
IRS 16NW (IR-Paumard)	—	—	$199 \pm 52$	$67 \pm 44$
IRS 16SE2 (7mm)	$6.63 \pm 1.06$	$2.26 \pm 2.09$	$265.4 \pm 42.4$	$90.3 \pm 83.5$
IRS 16SE2 (IR-Paumard)	—	—	$107 \pm 28$	$181 \pm 29$
IRS 16SW (7mm)	$4.95 \pm 1.79$	$1.61 \pm 4.06$	$198.0 \pm 71.4$	$64.4 \pm 162.5$
IRS 16SW (IR-Lu)	$6.80 \pm 0.05$	$2.22 \pm 0.06$	—	—
IRS 16SW (IR-Paumard)	—	—	$261 \pm 47$	$90 \pm 43$
IRS 34W (7mm)	$-0.81 \pm 1.01$	$-3.57 \pm 1.37$	$-32.4 \pm 40.6$	$-142.7 \pm 55.0$
IRS 34W (IR-Paumard)	—	—	$-79 \pm 28$	$-166 \pm 27$
AFNW (7mm)	$-3.89 \pm 0.95$	$-0.32 \pm 1.37$	$-155.8 \pm 38.1$	$-12.9 \pm 54.7$
AFNW (IR-Paumard)	—	—	$-67 \pm 28$	$-92 \pm 28$
AF (7mm)	$-2.40 \pm 0.83$	$8.14 \pm 1.31$	$-96.1 \pm 33.2$	$325.5 \pm 52.4$
AF (IR-Paumard)	—	—	$68 \pm 38$	$50 \pm 36$
SgrA* (7mm)	$0.000 \pm 0.000$	$0.000 \pm 0.000$	$0.0 \pm 0.0$	$0.0 \pm 0.0$

Table 3. Comparison of the absolute coordinates of the orbit-evolved NIR sources from Lu *et al.* (2009) at the epoch of radio data. Sgr A\*’s pixel position 3456.0×3456.0 with the pixel size 8.68159 mas.

Name	dX( $''$ ) ( $arcsec$ )	X <sub>error</sub> ( $arcsec$ )	dY( $''$ ) ( $arcsec$ )	Y <sub>error</sub> ( $arcsec$ )	X ( $pixel\ number$ )	Y ( $pixel\ number$ )
IRS 16NW	0.1086	$\pm 0.0009$	1.2352	$\pm 0.0033$	3445.73	3596.75
IRS 16C	1.0078	$\pm 0.0023$	0.5893	$\pm 0.0012$	3336.02	3520.02
IRS 16SW	1.1326	$\pm 0.0025$	-0.9334	$\pm 0.0023$	3325.75	3346.70
IRS 16NE	2.9041	$\pm 0.0034$	0.9068	$\pm 0.0015$	3121.91	3564.57
S3-5	2.9561	$\pm 0.0049$	-1.1374	$\pm 0.0022$	3115.41	3325.79
IRS 33E	0.7026	$\pm 0.0054$	-3.1266	$\pm 0.0107$	3371.53	3093.82

Table 4. Comparison of the absolute coordinates of the orbit-evolved NIR sources from Paumard *et al.* (2006) at the epoch of radio data.

Source number	Name	RA (IR) 17 <sup>h</sup> 45 <sup>m</sup>	Dec (IR) −29°00′	dX arcsec	dY arcsec	X (NIR) pixel number	Y (NIR) pixel number	X (Radio) pixel number	Y (Radio) pixel number
E19	IRS16NW	40 <sup>s</sup> .0442	26′.843	0.078	1.226	3447.015	3597.218	3443.671	3595.712
E20	IRS16C	40 <sup>s</sup> .1182	27′′.517	1.048	0.552	3335.285	3519.583	3339.503	3522.835
E23	IRS16SW	40 <sup>s</sup> .1231	29′′.027	1.113	−0.958	3327.798	3345.652	3324.467	3347.939
E25	W14	39 <sup>s</sup> .9182	28′′.588	−1.575	−0.519	3637.418	3396.218	3639.259	3398.188
E39	IRS16NE	40 <sup>s</sup> .2590	27′′.130	2.895	0.939	3122.536	3564.160	3121.024	3561.288
E40	IRS16SE2	40 <sup>s</sup> .2644	29′′.216	2.966	−1.147	3114.358	3323.881	3113.503	3326.325
E41	IRS33E	40 <sup>s</sup> .0912	31′′.191	0.694	−3.122	3376.061	3096.388	3371.388	3093.664
E51	IRS13E2	39 <sup>s</sup> .7934	29′′.793	−3.213	−1.724	3826.094	3257.419	3827.974	3257.590
E56	IRS34W	39 <sup>s</sup> .7281	26′′.519	−4.069	1.550	3924.693	3634.539	3925.664	3631.678
E58	IRS3E	39 <sup>s</sup> .8660	24′′.269	−2.260	3.800	3716.321	3893.708	3721.872	3895.693
E63	IRS1W	40 <sup>s</sup> .4380	27′′.449	5.244	0.620	2851.963	3527.415	2854.267	3526.253
E65	IRS9W	40 <sup>s</sup> .2586	33′′.657	2.890	−5.588	3123.112	2812.339	3119.869	2812.905
E66	IRS7SW	39 <sup>s</sup> .7371	23′′.165	−3.951	4.904	3911.101	4020.874	3910.743	4019.360
E70	IRS7E2	40 <sup>s</sup> .3782	23′′.101	4.459	4.968	2942.384	4028.245	2939.391	4026.572
E74	AFNW	39 <sup>s</sup> .4555	31′′.661	−7.646	−3.592	4336.714	3042.251	4334.515	3039.248
E79	AF	39 <sup>s</sup> .5410	34′′.967	−6.524	−6.898	4207.475	2661.445	4203.622	2662.343
E80	IRS9SE	40 <sup>s</sup> .4690	36′′.270	5.650	−8.201	2805.198	2511.357	2805.641	2511.060
E81	AFNWNW	39 <sup>s</sup> .3058	30′′.651	−9.609	−2.582	4562.825	3158.589	4560.840	3161.553
E82	Blum	39 <sup>s</sup> .3794	33′′.339	−8.643	−5.270	4451.555	2848.968	4450.125	2848.228
E83	IRS15SW	39 <sup>s</sup> .9169	18′′.057	−1.593	10.012	3639.492	4609.245	3638.251	4609.362
E88	IRS15NE	40 <sup>s</sup> .1433	16′′.364	1.378	11.705	3297.273	4804.255	3298.914	4803.245

Table 5. Derived mass loss rates from radio and NIR observations

IR Name	Velocity <sup>a</sup> (km s <sup>−1</sup> )	H/He	Z	$\dot{M}$ (NIR) (10 <sup>−5</sup> M <sub>⊙</sub> yr <sup>−1</sup> )	Flux <sup>b</sup> (34.5 GHz) (mJy)	$\dot{M}$ (34.5 GHz) (10 <sup>−5</sup> M <sub>⊙</sub> yr <sup>−1</sup> )	Flux <sup>b</sup> (44.6 GHz) (mJy)	$\dot{M}$ (44.6 GHz) (10 <sup>−5</sup> M <sub>⊙</sub> yr <sup>−1</sup> )
34W	650	4.0	1.33	1.32	0.480±0.015	1.28±0.03	0.580±0.038	1.31±0.02
IRS 16NW	600	5.0	1.29	1.12	0.228±0.015	0.66±0.03	0.245±0.037	0.62±0.03
IRS 16C	650	2.5	1.44	2.24	0.449±0.015	1.26±0.03	0.525±0.038	1.266±0.03
33E	450	0.26	1.33	1.58	0.258±0.014	0.55±0.02	0.341±0.038	0.61±0.02
AF	700	0.65	1.50	1.78	0.650±0.015	1.83±0.03	0.767±0.038	1.85±0.03
AFNW	800	0.39	1.95	3.16	0.391±0.015	1.63±0.03	0.476±0.038	1.68±0.04
IRS 16SE2	2500	0.32	0.04	7.08	0.325±0.015	4.49±0.15	0.367±0.038	4.38±0.13
IRS 15NE	800	0.26	2.0	1.99	0.265 ±0.015	1.23±0.05	0.370±0.038	1.41±0.04
IRS 9W	1100	0.1	1.95	4.47	0.201 ±0.014	1.36±0.07	0.331±0.038	1.76±0.05
IRS 7SW	900	0.0	2.0	1.99	0.146 ±0.015	0.89±0.07	0.143±0.037	0.78±0.06
AFNWNW	1800	0.1	1.95	1.22	0.234 ±0.015	2.50 ±0.01	0.290±0.038	2.61±0.10
IRS 16NE <sup>c</sup>	700	–	0.98	–	0.933±0.015	1.94±0.02	1.176±0.038	2.06±0.02
IRS 16SW <sup>c</sup>	700	–	0.98	–	0.242±0.015	0.70±0.03	0.297±0.038	0.73±0.03

<sup>a</sup>Terminal wind velocity

<sup>b</sup>Peak flux density

<sup>c</sup>Terminal velocity is not available and is assumed to be 700 km s<sup>−1</sup>

Table 6. Gaussian Fitted Parameters of 34.5 GHz Continuum Sources within 30'' of Sgr A\*

ID	Alt Name	RA (J2000)	Dec (J2000)	Dist. from Sgr A* (arcsec)	Pos. Precision (mas)	$\theta_a \times \theta_b$ (PA) mas $\times$ mas (deg)	Peak Intensity (mJy beam <sup>-1</sup> )	Integrated Flux (mJy)	Flux Ks (mJy)	Flux L' (mJy)	Refs & Comments
1	Sgr A*	17:45:40.0383	-29:00:28.0690	0.00	0.00	-	1719.700 $\pm$ 0.015	1722.900 $\pm$ 0.025	0.30 $\pm$ 0.016	1.47 $\pm$ 0.077	- -
2	-	17:45:40.0072	-29:00:28.0293	0.41	3.81	68 $\times$ 28(100)	0.144 $\pm$ 0.014	0.266 $\pm$ 0.037	-	0.91 $\pm$ 0.048	- a
3	IRS 16C	17:45:40.1152	-29:00:27.4849	1.17	1.24	19 $\times$ 7(16)	0.449 $\pm$ 0.015	0.465 $\pm$ 0.026	80.49 $\pm$ 4.003	138.05 $\pm$ 7.247	1 -
4	IRS 16NW	17:45:40.0463	-29:00:26.8493	1.22	2.23	21 $\times$ 0(24)	0.228 $\pm$ 0.015	0.215 $\pm$ 0.024	57.61 $\pm$ 2.865	97.29 $\pm$ 5.107	1 -
5	n4	17:45:40.0076	-29:00:29.2577	1.26	4.94	86 $\times$ 15(1)	0.150 $\pm$ 0.014	0.220 $\pm$ 0.032	0.17 $\pm$ 0.010	1.18 $\pm$ 0.062	- -
6	-	17:45:40.0216	-29:00:29.4645	1.41	3.46	103 $\times$ 53(75)	0.175 $\pm$ 0.014	0.494 $\pm$ 0.050	-	1.19 $\pm$ 0.062	- a
7	-	17:45:39.9576	-29:00:29.0822	1.47	7.25	103 $\times$ 42(162)	0.107 $\pm$ 0.014	0.228 $\pm$ 0.041	-	0.50 $\pm$ 0.026	- a
8	IRS 16SW	17:45:40.1255	-29:00:29.0013	1.48	2.52	48 $\times$ 8(17)	0.242 $\pm$ 0.014	0.287 $\pm$ 0.028	72.20 $\pm$ 3.591	116.32 $\pm$ 6.106	1 -
9	-	17:45:39.9237	-29:00:28.4777	1.56	2.05	-	0.181 $\pm$ 0.015	0.015 $\pm$ 0.006	-	-	- -
10	-	17:45:39.8934	-29:00:28.1997	1.91	2.69	63 $\times$ 49(34)	0.233 $\pm$ 0.014	0.428 $\pm$ 0.037	-	0.74 $\pm$ 0.039	- a
11	IRS 29	17:45:39.9214	-29:00:26.7143	2.05	9.79	54 $\times$ 23(2)	0.064 $\pm$ 0.014	0.084 $\pm$ 0.030	73.41 $\pm$ 3.651	596.01 $\pm$ 31.289	1 -
12	IRS 16CC	17:45:40.1891	-29:00:27.4488	2.07	12.51	95 $\times$ 33(175)	0.061 $\pm$ 0.014	0.110 $\pm$ 0.036	41.85 $\pm$ 2.082	60.60 $\pm$ 3.181	1 -
13	Magnetar	17:45:40.1680	-29:00:29.7501	2.39	0.44	30 $\times$ 0(156)	1.303 $\pm$ 0.015	1.390 $\pm$ 0.026	-	-	- -
14	-	17:45:39.9099	-29:00:29.7777	2.40	5.24	97 $\times$ 43(142)	0.133 $\pm$ 0.014	0.297 $\pm$ 0.042	-	-	- -
15	-	17:45:39.9108	-29:00:26.3431	2.40	7.55	58 $\times$ 0(160)	0.084 $\pm$ 0.014	0.104 $\pm$ 0.029	-	-	- -
16	-	17:45:39.9312	-29:00:30.2056	2.56	7.87	85 $\times$ 0(36)	0.085 $\pm$ 0.014	0.137 $\pm$ 0.034	-	-	- -
17	n8	17:45:39.9088	-29:00:30.3123	2.81	3.80	62 $\times$ 0(127)	0.127 $\pm$ 0.015	0.001 $\pm$ 0.002	3.70 $\pm$ 0.187	6.24 $\pm$ 0.327	- -
18	-	17:45:39.8329	-29:00:28.9084	2.82	2.95	107 $\times$ 80(126)	0.244 $\pm$ 0.013	0.805 $\pm$ 0.056	-	-	- -
19	-	17:45:39.9456	-29:00:30.7269	2.92	1.44	156 $\times$ 0(75)	0.219 $\pm$ 0.015	0.081 $\pm$ 0.014	-	-	- -
20	-	17:45:39.8379	-29:00:29.4185	2.96	1.28	157 $\times$ 60(16)	0.783 $\pm$ 0.013	2.661 $\pm$ 0.057	-	-	- -
21	IRS 13N- $\delta$	17:45:39.8163	-29:00:28.8580	3.02	0.75	127 $\times$ 83(110)	0.944 $\pm$ 0.013	3.726 $\pm$ 0.064	0.16 $\pm$ 0.010	12.36 $\pm$ 0.649	2 -
22	IRS 16NE	17:45:40.2600	-29:00:27.1540	3.05	0.60	19 $\times$ 11(151)	0.933 $\pm$ 0.015	0.987 $\pm$ 0.026	148.77 $\pm$ 7.399	266.96 $\pm$ 14.015	1 -
23	IRS 13N- $\alpha$	17:45:39.8326	-29:00:29.5086	3.06	1.24	117 $\times$ 77(139)	0.617 $\pm$ 0.013	2.080 $\pm$ 0.057	0.20 $\pm$ 0.011	-	2 b
24	-	17:45:39.8102	-29:00:28.7058	3.06	3.45	116 $\times$ 42(152)	0.230 $\pm$ 0.014	0.550 $\pm$ 0.044	-	-	- -
25	IRS 13N- $\beta$	17:45:39.8179	-29:00:29.2564	3.13	1.31	113 $\times$ 70(164)	0.614 $\pm$ 0.014	1.810 $\pm$ 0.051	0.30 $\pm$ 0.016	13.52 $\pm$ 0.710	2 -
26	-	17:45:39.7990	-29:00:28.5348	3.17	2.73	138 $\times$ 75(138)	0.300 $\pm$ 0.013	1.132 $\pm$ 0.062	-	-	- -
27	-	17:45:39.8069	-29:00:28.9758	3.17	1.66	104 $\times$ 66(28)	0.454 $\pm$ 0.014	1.264 $\pm$ 0.049	-	-	- -
28	IRS 35	17:45:40.2648	-29:00:29.1993	3.18	1.80	40 $\times$ 22(153)	0.325 $\pm$ 0.014	0.404 $\pm$ 0.029	11.80 $\pm$ 0.587	27.55 $\pm$ 1.446	1 -
29	-	17:45:39.8210	-29:00:29.4799	3.18	1.47	88 $\times$ 51(129)	0.442 $\pm$ 0.014	1.030 $\pm$ 0.043	0.12 $\pm$ 0.006	-	- b
30	-	17:45:39.8165	-29:00:29.4354	3.21	2.00	91 $\times$ 52(168)	0.367 $\pm$ 0.014	0.795 $\pm$ 0.041	-	-	- -
31	IRS 33SE	17:45:40.0941	-29:00:31.2151	3.23	2.52	68 $\times$ 23(22)	0.258 $\pm$ 0.014	0.382 $\pm$ 0.032	58.47 $\pm$ 2.908	96.75 $\pm$ 5.079	1 -
32	IRS 33SW	17:45:40.0148	-29:00:31.2840	3.23	4.79	148 $\times$ 90(4)	0.202 $\pm$ 0.013	0.854 $\pm$ 0.068	24.67 $\pm$ 1.227	40.41 $\pm$ 2.121	1 -
33	-	17:45:39.7922	-29:00:28.3776	3.24	2.30	166 $\times$ 101(93)	0.326 $\pm$ 0.013	1.828 $\pm$ 0.086	-	-	- -
34	-	17:45:39.9079	-29:00:30.8415	3.26	2.20	90 $\times$ 71(60)	0.306 $\pm$ 0.014	0.843 $\pm$ 0.049	-	-	- -
35	IRS 13N- $\kappa$	17:45:39.7961	-29:00:28.8174	3.26	2.56	120 $\times$ 27(115)	0.235 $\pm$ 0.014	0.639 $\pm$ 0.049	-	7.94 $\pm$ 0.417	2 a
36	-	17:45:39.8056	-29:00:29.2515	3.27	1.02	108 $\times$ 58(59)	0.651 $\pm$ 0.014	1.891 $\pm$ 0.051	0.55 $\pm$ 0.027	-	- b
37	IRS 13N- $\gamma$	17:45:39.7986	-29:00:29.0012	3.28	1.36	100 $\times$ 82(176)	0.561 $\pm$ 0.013	1.716 $\pm$ 0.053	0.53 $\pm$ 0.030	-	2 b
38	-	17:45:39.8247	-29:00:29.7828	3.28	0.57	125 $\times$ 93(25)	1.480 $\pm$ 0.013	5.828 $\pm$ 0.064	-	-	- -
39	-	17:45:39.7874	-29:00:28.5065	3.32	1.44	77 $\times$ 66(127)	0.455 $\pm$ 0.014	1.078 $\pm$ 0.044	-	-	- -
40	-	17:45:39.7918	-29:00:28.8128	3.32	2.40	60 $\times$ 0(180)	0.218 $\pm$ 0.014	0.354 $\pm$ 0.034	-	-	- -
41	-	17:45:40.1882	-29:00:30.7867	3.35	6.55	122 $\times$ 109(26)	0.128 $\pm$ 0.013	0.558 $\pm$ 0.070	-	-	- -
42	-	17:45:39.7993	-29:00:29.2826	3.36	1.45	63 $\times$ 55(119)	0.424 $\pm$ 0.014	0.832 $\pm$ 0.038	-	-	- -
43	-	17:45:39.7837	-29:00:28.3883	3.36	2.25	99 $\times$ 67(166)	0.338 $\pm$ 0.014	0.893 $\pm$ 0.048	-	-	- -
44	-	17:45:40.0964	-29:00:31.3526	3.37	3.20	26 $\times$ 0(172)	0.165 $\pm$ 0.015	0.182 $\pm$ 0.027	-	-	- -
45	-	17:45:39.8474	-29:00:30.4173	3.43	3.05	147 $\times$ 72(76)	0.219 $\pm$ 0.013	0.933 $\pm$ 0.068	0.09 $\pm$ 0.004	-	- b
46	-	17:45:39.8212	-29:00:29.9818	3.43	0.35	-	0.542 $\pm$ 0.015	0.071 $\pm$ 0.008	-	-	- -
47	-	17:45:39.7868	-29:00:29.0695	3.45	2.97	69 $\times$ 53(179)	0.223 $\pm$ 0.014	0.430 $\pm$ 0.038	0.05 $\pm$ 0.003	-	- b
48	-	17:45:40.2093	-29:00:30.7183	3.47	0.72	139 $\times$ 89(83)	0.991 $\pm$ 0.013	4.441 $\pm$ 0.071	-	-	- -



Table 6—Continued

ID	Alt Name	RA (J2000)	Dec (J2000)	Dist. from Sgr A* (arcsec)	Pos. Precision (mas)	$\theta_a \times \theta_b$ (PA) mas $\times$ mas (deg)	Peak Intensity (mJy beam <sup>-1</sup> )	Integrated Flux (mJy)	Flux Ks (mJy)	Flux L' (mJy)	Refs & Comments
49	-	17:45:39.8095	-29:00:29.8291	3.48	0.91	116 $\times$ 84(21)	0.892 $\pm$ 0.013	3.079 $\pm$ 0.058	-	-	- -
50	-	17:45:40.2193	-29:00:30.6437	3.50	0.66	-	0.553 $\pm$ 0.015	0.043 $\pm$ 0.006	-	-	- -
51	-	17:45:39.9345	-29:00:31.2941	3.50	2.06	144 $\times$ 99(4)	0.461 $\pm$ 0.013	2.081 $\pm$ 0.072	-	1.64 $\pm$ 0.086	- a
52	IRS 21	17:45:40.2175	-29:00:30.7427	3.56	0.04	12 $\times$ 0(89)	0.805 $\pm$ 0.015	0.044 $\pm$ 0.005	41.51 $\pm$ 2.064	-	1 b
53	IRS 13-E3c	17:45:39.7933	-29:00:29.6178	3.57	0.16	112 $\times$ 89(37)	4.913 $\pm$ 0.013	17.447 $\pm$ 0.059	5.36 $\pm$ 0.336	233.37 $\pm$ 12.251	2 -
54	IRS 13-E3N	17:45:39.7878	-29:00:29.4705	3.57	0.66	89 $\times$ 48(128)	0.975 $\pm$ 0.014	2.241 $\pm$ 0.043	14.42 $\pm$ 0.730	97.47 $\pm$ 5.117	2 -
55	-	17:45:40.2121	-29:00:30.8404	3.59	0.95	108 $\times$ 71(140)	0.777 $\pm$ 0.013	2.353 $\pm$ 0.052	-	-	- -
56	-	17:45:40.2233	-29:00:30.7224	3.60	1.17	144 $\times$ 114(10)	0.806 $\pm$ 0.013	4.080 $\pm$ 0.079	-	-	- -
57	IRS 21	17:45:40.2171	-29:00:30.8244	3.62	0.01	-	0.704 $\pm$ 0.015	0.002 $\pm$ 0.001	-	496.19 $\pm$ 26.049	1 a
58	n17	17:45:39.9929	-29:00:31.6362	3.62	3.27	97 $\times$ 86(170)	0.229 $\pm$ 0.013	0.712 $\pm$ 0.054	0.15 $\pm$ 0.009	1.37 $\pm$ 0.072	- -
59	-	17:45:40.2063	-29:00:30.9615	3.64	9.09	155 $\times$ 72(10)	0.110 $\pm$ 0.013	0.411 $\pm$ 0.062	-	-	- -
60	-	17:45:40.2200	-29:00:30.8343	3.65	1.65	166 $\times$ 126(49)	0.574 $\pm$ 0.013	3.628 $\pm$ 0.095	-	-	- -
61	IRS 13-E5	17:45:39.7776	-29:00:29.5497	3.73	0.48	92 $\times$ 60(23)	1.505 $\pm$ 0.014	3.654 $\pm$ 0.045	1.15 $\pm$ 0.060	41.69 $\pm$ 2.189	2 -
62	-	17:45:39.7683	-29:00:29.4468	3.80	2.14	68 $\times$ 54(173)	0.306 $\pm$ 0.014	0.594 $\pm$ 0.038	-	-	- -
63	n19	17:45:40.3112	-29:00:26.5384	3.89	3.39	95 $\times$ 84(99)	0.206 $\pm$ 0.013	0.646 $\pm$ 0.054	0.09 $\pm$ 0.006	4.40 $\pm$ 0.231	- -
64	-	17:45:39.7944	-29:00:30.4545	3.99	1.72	325 $\times$ 91(3)	1.084 $\pm$ 0.013	9.082 $\pm$ 0.121	0.09 $\pm$ 0.005	-	- b
65	-	17:45:39.7597	-29:00:29.7418	4.02	1.23	112 $\times$ 49(116)	0.516 $\pm$ 0.014	1.474 $\pm$ 0.050	-	-	- -
66	n20	17:45:40.3272	-29:00:26.4595	4.12	4.35	97 $\times$ 90(79)	0.165 $\pm$ 0.013	0.546 $\pm$ 0.056	6.32 $\pm$ 0.314	8.20 $\pm$ 0.430	- -
67	-	17:45:39.7451	-29:00:26.5452	4.14	4.26	213 $\times$ 58(146)	0.263 $\pm$ 0.013	1.226 $\pm$ 0.073	0.15 $\pm$ 0.009	-	- b
68	-	17:45:39.7664	-29:00:25.8938	4.18	3.46	271 $\times$ 173(150)	0.379 $\pm$ 0.012	4.738 $\pm$ 0.156	0.04 $\pm$ 0.002	-	- b
69	-	17:45:39.7515	-29:00:29.9388	4.20	1.37	-	0.273 $\pm$ 0.015	0.023 $\pm$ 0.006	-	-	- -
70	-	17:45:39.7562	-29:00:30.1631	4.25	1.75	-	0.273 $\pm$ 0.015	0.009 $\pm$ 0.004	0.05 $\pm$ 0.003	-	- b
71	IRS 34W	17:45:39.7275	-29:00:26.5423	4.35	1.11	31 $\times$ 0(26)	0.481 $\pm$ 0.015	0.526 $\pm$ 0.027	21.39 $\pm$ 1.064	49.16 $\pm$ 2.581	3 -
72	IRS 3	17:45:39.8620	-29:00:24.2480	4.47	9.71	94 $\times$ 0(148)	0.074 $\pm$ 0.014	0.093 $\pm$ 0.029	20.84 $\pm$ 1.037	1252.14 $\pm$ 65.733	4 -
73	-	17:45:39.7488	-29:00:30.6291	4.58	2.20	173 $\times$ 45(14)	0.490 $\pm$ 0.013	1.546 $\pm$ 0.054	0.05 $\pm$ 0.002	-	- b
74	-	17:45:40.2378	-29:00:31.8304	4.58	7.54	72 $\times$ 49(59)	0.081 $\pm$ 0.014	0.167 $\pm$ 0.040	-	-	- -
75	-	17:45:40.3273	-29:00:25.3226	4.68	12.38	305 $\times$ 0(104)	0.039 $\pm$ 0.015	0.001 $\pm$ 0.003	-	-	- -
76	-	17:45:39.7299	-29:00:30.5161	4.73	3.14	70 $\times$ 53(150)	0.206 $\pm$ 0.014	0.408 $\pm$ 0.039	-	-	- -
77	IRS 34NW	17:45:39.7494	-29:00:25.2459	4.73	18.67	53 $\times$ 13(134)	0.031 $\pm$ 0.014	0.043 $\pm$ 0.031	3.65 $\pm$ 0.185	6.05 $\pm$ 0.318	3 -
78	-	17:45:40.2622	-29:00:31.7715	4.73	8.94	89 $\times$ 41(170)	0.082 $\pm$ 0.014	0.157 $\pm$ 0.038	-	-	- -
79	-	17:45:39.7494	-29:00:25.2458	4.73	18.54	54 $\times$ 14(131)	0.031 $\pm$ 0.014	0.044 $\pm$ 0.031	-	-	- -
80	-	17:45:39.7422	-29:00:31.1574	4.96	1.26	140 $\times$ 109(149)	0.710 $\pm$ 0.013	3.432 $\pm$ 0.076	0.06 $\pm$ 0.003	-	- b
81	-	17:45:39.7276	-29:00:25.2467	4.96	8.98	102 $\times$ 28(145)	0.080 $\pm$ 0.014	0.163 $\pm$ 0.040	-	-	- -
82	-	17:45:39.7275	-29:00:25.2450	4.96	10.13	125 $\times$ 56(148)	0.080 $\pm$ 0.014	0.230 $\pm$ 0.051	-	-	- -
83	-	17:45:40.2748	-29:00:32.0907	5.08	17.69	168 $\times$ 43(159)	0.058 $\pm$ 0.013	0.180 $\pm$ 0.053	-	-	- -
84	-	17:45:39.6380	-29:00:28.1141	5.25	2.93	243 $\times$ 83(73)	0.261 $\pm$ 0.013	1.878 $\pm$ 0.106	-	0.96 $\pm$ 0.050	- a
85	IRS 1W	17:45:40.4362	-29:00:27.4499	5.26	0.53	-	0.443 $\pm$ 0.015	0.083 $\pm$ 0.009	80.86 $\pm$ 4.021	554.69 $\pm$ 29.120	4 -
86	-	17:45:39.6831	-29:00:25.5558	5.29	7.25	182 $\times$ 65(153)	0.146 $\pm$ 0.013	0.603 $\pm$ 0.067	-	-	- -
87	-	17:45:39.6561	-29:00:26.0476	5.41	5.57	95 $\times$ 17(156)	0.132 $\pm$ 0.014	0.224 $\pm$ 0.035	-	-	- -
88	-	17:45:39.6226	-29:00:26.5877	5.65	1.02	118 $\times$ 76(114)	0.678 $\pm$ 0.013	2.390 $\pm$ 0.059	-	1.89 $\pm$ 0.099	- a
89	n25	17:45:40.1050	-29:00:22.2313	5.90	4.36	39 $\times$ 0(151)	0.134 $\pm$ 0.015	0.146 $\pm$ 0.027	13.32 $\pm$ 0.662	23.97 $\pm$ 1.258	- -
90	-	17:45:39.5712	-29:00:29.0089	6.20	8.30	588 $\times$ 163(10)	0.249 $\pm$ 0.008	6.113 $\pm$ 0.212	-	-	- -
91	IRS 9W	17:45:40.2609	-29:00:33.6449	6.29	2.98	44 $\times$ 16(19)	0.201 $\pm$ 0.014	0.244 $\pm$ 0.028	10.16 $\pm$ 0.515	19.50 $\pm$ 1.024	3 -
92	IRS 7SW	17:45:39.7371	-29:00:23.1803	6.29	3.41	-	0.146 $\pm$ 0.015	0.126 $\pm$ 0.023	7.40 $\pm$ 0.368	12.16 $\pm$ 0.638	3 -
93	-	17:45:39.6189	-29:00:31.5673	6.52	8.89	105 $\times$ 58(24)	0.086 $\pm$ 0.014	0.221 $\pm$ 0.047	-	0.11 $\pm$ 0.006	- a
94	-	17:45:39.5481	-29:00:26.3898	6.65	4.71	260 $\times$ 20(3)	0.331 $\pm$ 0.013	1.127 $\pm$ 0.057	-	-	- -
95	-	17:45:39.5658	-29:00:25.6191	6.67	9.35	234 $\times$ 105(8)	0.147 $\pm$ 0.013	1.035 $\pm$ 0.104	-	-	- -
96	n28	17:45:40.1550	-29:00:21.5389	6.71	10.88	63 $\times$ 0(33)	0.057 $\pm$ 0.014	0.069 $\pm$ 0.028	1.33 $\pm$ 0.070	3.99 $\pm$ 0.209	- -
97	-	17:45:39.6574	-29:00:23.3315	6.89	7.62	34 $\times$ 0(17)	0.068 $\pm$ 0.015	0.076 $\pm$ 0.027	-	-	- -

Table 6—Continued

ID	Alt Name	RA (J2000)	Dec (J2000)	Dist. from Sgr A*	Pos. Precision	$\theta_a \times \theta_b$ (PA)	Peak Intensity	Integrated Flux	Flux Ks	Flux L'	Refs & Comments
				(arcsec)	(mas)	mas $\times$ mas (deg)	(mJy beam <sup>-1</sup> )	(mJy)	(mJy)	(mJy)	
98	-	17:45:39.5534	-29:00:24.9464	7.09	5.10	215 $\times$ 201(102)	0.220 $\pm$ 0.012	2.584 $\pm$ 0.152	-	-	--
99	-	17:45:39.5276	-29:00:25.5663	7.15	5.70	319 $\times$ 149(7)	0.285 $\pm$ 0.012	3.578 $\pm$ 0.157	-	-	--
100	-	17:45:40.5213	-29:00:24.0860	7.48	16.01	120 $\times$ 25(38)	0.047 $\pm$ 0.014	0.111 $\pm$ 0.044	-	-	--
101	-	17:45:39.4794	-29:00:26.4570	7.51	3.71	158 $\times$ 87(2)	0.275 $\pm$ 0.013	1.190 $\pm$ 0.069	-	-	--
102	-	17:45:40.2035	-29:00:20.7599	7.62	7.72	54 $\times$ 0(44)	0.073 $\pm$ 0.015	0.072 $\pm$ 0.025	-	-	--
103	-	17:45:39.4983	-29:00:24.9954	7.72	7.88	217 $\times$ 191(157)	0.153 $\pm$ 0.012	1.711 $\pm$ 0.149	-	-	--
104	-	17:45:39.4390	-29:00:28.1584	7.86	11.91	330 $\times$ 117(15)	0.150 $\pm$ 0.013	1.576 $\pm$ 0.145	0.03 $\pm$ 0.001	-	- b
105	-	17:45:39.5412	-29:00:23.5811	7.92	23.60	289 $\times$ 127(144)	0.060 $\pm$ 0.013	0.618 $\pm$ 0.144	-	-	--
106	-	17:45:40.5607	-29:00:32.0865	7.94	7.41	131 $\times$ 23(45)	0.100 $\pm$ 0.014	0.265 $\pm$ 0.047	-	-	--
107	-	17:45:39.4510	-29:00:25.9187	8.00	10.70	106 $\times$ 63(36)	0.069 $\pm$ 0.014	0.192 $\pm$ 0.049	-	1.94 $\pm$ 0.102	- a
108	-	17:45:40.5187	-29:00:33.0163	8.01	10.47	79 $\times$ 59(160)	0.065 $\pm$ 0.014	0.143 $\pm$ 0.042	-	-	--
109	-	17:45:40.4671	-29:00:22.1546	8.16	5.85	89 $\times$ 73(128)	0.117 $\pm$ 0.014	0.317 $\pm$ 0.049	-	-	--
110	AFNW	17:45:39.4569	-29:00:31.6843	8.44	1.38	9 $\times$ 0(19)	0.391 $\pm$ 0.015	0.387 $\pm$ 0.025	15.18 $\pm$ 0.755	24.78 $\pm$ 1.301	3 -
111	-	17:45:40.5908	-29:00:23.5846	8.52	17.04	71 $\times$ 43(46)	0.037 $\pm$ 0.014	0.070 $\pm$ 0.038	-	-	--
112	-	17:45:39.4848	-29:00:32.7037	8.61	26.17	151 $\times$ 93(114)	0.029 $\pm$ 0.013	0.143 $\pm$ 0.076	-	-	--
113	n30	17:45:39.9455	-29:00:36.6367	8.65	13.84	171 $\times$ 41(141)	0.066 $\pm$ 0.013	0.228 $\pm$ 0.058	0.46 $\pm$ 0.025	0.54 $\pm$ 0.029	--
114	-	17:45:39.9360	-29:00:36.6238	8.66	7.81	40 $\times$ 0(9)	0.063 $\pm$ 0.014	0.075 $\pm$ 0.028	-	-	--
115	-	17:45:39.9395	-29:00:36.6614	8.69	10.48	137 $\times$ 21(110)	0.056 $\pm$ 0.013	0.172 $\pm$ 0.053	-	-	--
116	-	17:45:39.3677	-29:00:28.0994	8.80	10.53	185 $\times$ 41(154)	0.102 $\pm$ 0.013	0.345 $\pm$ 0.057	-	-	--
117	-	17:45:39.9039	-29:00:36.7861	8.89	14.84	98 $\times$ 81(2)	0.051 $\pm$ 0.014	0.153 $\pm$ 0.052	-	-	--
118	-	17:45:40.4043	-29:00:20.5582	8.91	4.82	95 $\times$ 67(132)	0.143 $\pm$ 0.014	0.389 $\pm$ 0.048	-	-	--
119	-	17:45:40.6562	-29:00:24.0843	9.03	18.75	97 $\times$ 56(43)	0.037 $\pm$ 0.014	0.093 $\pm$ 0.046	-	-	--
120	-	17:45:39.6671	-29:00:20.4283	9.06	22.21	259 $\times$ 132(24)	0.064 $\pm$ 0.013	0.610 $\pm$ 0.136	-	-	--
121	-	17:45:39.8385	-29:00:19.2736	9.18	4.56	56 $\times$ 45(12)	0.136 $\pm$ 0.014	0.224 $\pm$ 0.034	-	-	--
122	-	17:45:39.3419	-29:00:29.0936	9.19	12.65	132 $\times$ 57(12)	0.071 $\pm$ 0.014	0.206 $\pm$ 0.051	-	-	--
123	-	17:45:40.4140	-29:00:20.1767	9.30	9.31	233 $\times$ 142(138)	0.128 $\pm$ 0.013	1.191 $\pm$ 0.133	-	0.09 $\pm$ 0.005	- a
124	n31	17:45:40.7579	-29:00:27.8216	9.44	6.72	57 $\times$ 0(130)	0.084 $\pm$ 0.014	0.102 $\pm$ 0.028	4.85 $\pm$ 0.246	6.40 $\pm$ 0.336	--
125	-	17:45:40.4068	-29:00:19.9339	9.46	2.56	111 $\times$ 38(130)	0.264 $\pm$ 0.014	0.665 $\pm$ 0.046	-	-	--
126	AF/AHH	17:45:39.5435	-29:00:34.9596	9.47	0.86	21 $\times$ 13(1)	0.650 $\pm$ 0.015	0.694 $\pm$ 0.026	31.84 $\pm$ 1.583	58.35 $\pm$ 3.063	3 -
127	-	17:45:39.4133	-29:00:32.8689	9.50	5.15	63 $\times$ 0(174)	0.097 $\pm$ 0.014	0.153 $\pm$ 0.033	-	-	--
128	-	17:45:40.5946	-29:00:21.9641	9.51	17.78	116 $\times$ 61(7)	0.047 $\pm$ 0.014	0.128 $\pm$ 0.049	-	-	--
129	-	17:45:39.4472	-29:00:33.6588	9.56	13.43	33 $\times$ 0(129)	0.040 $\pm$ 0.015	0.037 $\pm$ 0.024	-	0.10 $\pm$ 0.005	--
130	-	17:45:39.5727	-29:00:20.6684	9.60	25.23	430 $\times$ 107(21)	0.080 $\pm$ 0.012	1.022 $\pm$ 0.158	-	-	--
131	-	17:45:40.6861	-29:00:23.5839	9.61	4.29	78 $\times$ 30(101)	0.129 $\pm$ 0.014	0.262 $\pm$ 0.039	-	-	--
132	-	17:45:39.5760	-29:00:20.5667	9.65	14.58	192 $\times$ 69(15)	0.080 $\pm$ 0.013	0.350 $\pm$ 0.070	-	-	--
133	n33	17:45:39.8331	-29:00:18.8059	9.65	26.38	230 $\times$ 71(138)	0.042 $\pm$ 0.013	0.238 $\pm$ 0.087	0.35 $\pm$ 0.019	0.21 $\pm$ 0.013	--
134	-	17:45:40.4578	-29:00:20.1335	9.66	9.40	81 $\times$ 39(171)	0.075 $\pm$ 0.014	0.133 $\pm$ 0.036	-	-	--
135	-	17:45:40.4182	-29:00:19.5835	9.84	8.74	207 $\times$ 126(43)	0.123 $\pm$ 0.013	0.944 $\pm$ 0.112	-	-	--
136	-	17:45:40.4571	-29:00:19.8616	9.88	8.51	85 $\times$ 57(54)	0.076 $\pm$ 0.014	0.182 $\pm$ 0.044	-	-	--
137	-	17:45:39.7029	-29:00:19.1808	9.92	13.77	146 $\times$ 125(27)	0.068 $\pm$ 0.013	0.378 $\pm$ 0.085	-	-	--
138	AFNWNW	17:45:39.3070	-29:00:30.6316	9.93	2.35	17 $\times$ 0(39)	0.234 $\pm$ 0.015	0.238 $\pm$ 0.026	8.26 $\pm$ 0.418	15.68 $\pm$ 0.823	3 -
139	-	17:45:40.6251	-29:00:21.7848	9.94	25.12	76 $\times$ 65(119)	0.026 $\pm$ 0.014	0.060 $\pm$ 0.043	-	-	--
140	-	17:45:39.2976	-29:00:30.3461	9.98	36.95	242 $\times$ 95(149)	0.035 $\pm$ 0.013	0.238 $\pm$ 0.102	-	-	--
141	-	17:45:40.4351	-29:00:19.5028	10.02	4.01	189 $\times$ 124(86)	0.211 $\pm$ 0.013	1.522 $\pm$ 0.106	-	0.12 $\pm$ 0.007	- a
142	-	17:45:39.2749	-29:00:27.2890	10.04	1.71	81 $\times$ 58(173)	0.409 $\pm$ 0.014	0.884 $\pm$ 0.041	0.05 $\pm$ 0.003	-	- b
143	-	17:45:39.3973	-29:00:33.6179	10.07	26.78	347 $\times$ 208(16)	0.053 $\pm$ 0.010	0.981 $\pm$ 0.186	-	-	--
144	-	17:45:39.2689	-29:00:28.0515	10.09	5.28	121 $\times$ 59(26)	0.154 $\pm$ 0.014	0.445 $\pm$ 0.051	-	-	--
145	Blum	17:45:39.3800	-29:00:33.3474	10.12	8.64	22 $\times$ 0(151)	0.064 $\pm$ 0.015	0.057 $\pm$ 0.023	4.59 $\pm$ 0.232	6.84 $\pm$ 0.359	3 -
146	IRS 15SW	17:45:39.9178	-29:00:18.0503	10.14	3.40	-	0.142 $\pm$ 0.015	0.118 $\pm$ 0.022	12.15 $\pm$ 0.615	15.76 $\pm$ 0.828	3 -

Table 6—Continued

ID	Alt Name	RA (J2000)	Dec (J2000)	Dist. from Sgr A*	Pos. Precision	$\theta_a \times \theta_b$ (PA)	Peak Intensity	Integrated Flux	Flux Ks	Flux L'	Refs & Comments
				(arcsec)	(mas)	mas $\times$ mas (deg)	(mJy beam $^{-1}$ )	(mJy)	(mJy)	(mJy)	
147	-	17:45:40.1416	-29:00:18.0117	10.15	220.18	9950 $\times$ 0(50)	0.041 $\pm$ 0.003	6.251 $\pm$ 0.511	-	-	--
148	-	17:45:40.3945	-29:00:18.7981	10.38	4.78	122 $\times$ 40(137)	0.154 $\pm$ 0.014	0.408 $\pm$ 0.047	-	0.10 $\pm$ 0.005	- a
149	-	17:45:39.2453	-29:00:27.4434	10.42	3.20	245 $\times$ 189(79)	0.324 $\pm$ 0.012	4.085 $\pm$ 0.157	-	-	--
150	-	17:45:39.2708	-29:00:25.0090	10.52	4.89	62 $\times$ 21(72)	0.112 $\pm$ 0.014	0.190 $\pm$ 0.035	-	-	--
151	-	17:45:39.2262	-29:00:28.2596	10.66	7.55	10330 $\times$ 0(102)	0.425 $\pm$ 0.003	59.290 $\pm$ 0.489	-	-	--
152	-	17:45:39.2635	-29:00:24.8139	10.67	7.97	181 $\times$ 85(177)	0.142 $\pm$ 0.013	0.673 $\pm$ 0.075	-	0.11 $\pm$ 0.006	- a
153	-	17:45:40.4368	-29:00:18.5960	10.82	4.21	122 $\times$ 14(118)	0.145 $\pm$ 0.014	0.380 $\pm$ 0.047	-	-	--
154	-	17:45:39.9449	-29:00:17.3037	10.83	13.58	133 $\times$ 119(4)	0.066 $\pm$ 0.013	0.325 $\pm$ 0.077	-	-	--
155	-	17:45:39.2117	-29:00:27.6703	10.85	32.75	957 $\times$ 61(7)	0.120 $\pm$ 0.010	2.163 $\pm$ 0.184	-	-	--
156	-	17:45:39.8886	-29:00:17.2578	10.99	20.35	159 $\times$ 114(102)	0.040 $\pm$ 0.013	0.234 $\pm$ 0.089	-	-	--
157	-	17:45:39.2409	-29:00:23.7826	11.30	14.83	188 $\times$ 126(170)	0.077 $\pm$ 0.013	0.525 $\pm$ 0.101	-	-	--
158	-	17:45:40.7220	-29:00:21.0700	11.38	0.20	120 $\times$ 0(89)	0.098 $\pm$ 0.015	0.004 $\pm$ 0.004	-	-	--
159	-	17:45:39.1603	-29:00:28.1764	11.52	6.51	235 $\times$ 144(81)	0.145 $\pm$ 0.013	1.427 $\pm$ 0.140	-	-	--
160	-	17:45:39.2284	-29:00:23.5970	11.53	8.66	161 $\times$ 44(26)	0.113 $\pm$ 0.013	0.353 $\pm$ 0.054	-	-	--
161	-	17:45:39.1555	-29:00:27.8122	11.58	15.82	289 $\times$ 79(13)	0.104 $\pm$ 0.013	0.712 $\pm$ 0.102	-	-	--
162	IRS 15NE	17:45:40.1423	-29:00:16.3713	11.78	2.14	31 $\times$ 0(145)	0.265 $\pm$ 0.015	0.285 $\pm$ 0.026	14.10 $\pm$ 0.714	23.06 $\pm$ 1.211	3 -
163	-	17:45:39.1649	-29:00:25.2529	11.80	12.45	170 $\times$ 46(6)	0.087 $\pm$ 0.013	0.269 $\pm$ 0.053	-	-	--
164	n38	17:45:40.9554	-29:00:27.8892	12.03	14.40	232 $\times$ 48(27)	0.088 $\pm$ 0.013	0.395 $\pm$ 0.071	0.15 $\pm$ 0.008	0.17 $\pm$ 0.011	--
165	-	17:45:40.1836	-29:00:16.1777	12.04	12.79	121 $\times$ 106(85)	0.061 $\pm$ 0.013	0.265 $\pm$ 0.070	-	0.07 $\pm$ 0.004	- a
166	-	17:45:39.1207	-29:00:27.7423	12.04	16.11	268 $\times$ 121(30)	0.088 $\pm$ 0.013	0.806 $\pm$ 0.132	-	-	--
167	-	17:45:39.1206	-29:00:27.7443	12.04	15.51	252 $\times$ 119(28)	0.088 $\pm$ 0.013	0.746 $\pm$ 0.123	-	-	--
168	-	17:45:40.4443	-29:00:17.2614	12.05	12.66	186 $\times$ 141(90)	0.073 $\pm$ 0.013	0.563 $\pm$ 0.113	-	-	--
169	-	17:45:40.4442	-29:00:17.2611	12.05	12.27	158 $\times$ 133(78)	0.073 $\pm$ 0.013	0.463 $\pm$ 0.096	-	-	--
170	-	17:45:39.1166	-29:00:29.4422	12.17	22.24	117 $\times$ 19(41)	0.033 $\pm$ 0.014	0.075 $\pm$ 0.043	-	-	--
171	-	17:45:40.8327	-29:00:34.3871	12.19	5.79	226 $\times$ 90(44)	0.188 $\pm$ 0.013	1.229 $\pm$ 0.098	-	-	--
172	-	17:45:40.9771	-29:00:28.0832	12.31	15.58	259 $\times$ 227(14)	0.078 $\pm$ 0.011	1.197 $\pm$ 0.171	-	-	--
173	-	17:45:40.4553	-29:00:16.9167	12.42	9.37	211 $\times$ 135(10)	0.134 $\pm$ 0.013	1.064 $\pm$ 0.116	-	-	--
174	-	17:45:39.8825	-29:00:15.7784	12.46	24.58	72 $\times$ 30(179)	0.028 $\pm$ 0.014	0.042 $\pm$ 0.033	-	-	--
175	-	17:45:39.8825	-29:00:15.7810	12.46	25.06	74 $\times$ 22(2)	0.028 $\pm$ 0.014	0.040 $\pm$ 0.032	-	-	--
176	-	17:45:40.3477	-29:00:16.0054	12.73	9.49	106 $\times$ 79(117)	0.074 $\pm$ 0.013	0.241 $\pm$ 0.056	-	-	--
177	-	17:45:41.0086	-29:00:27.9045	12.73	22.91	348 $\times$ 212(25)	0.059 $\pm$ 0.009	1.130 $\pm$ 0.189	-	-	--
178	-	17:45:40.3590	-29:00:15.9615	12.82	13.24	88 $\times$ 0(46)	0.048 $\pm$ 0.014	0.084 $\pm$ 0.036	-	-	--
179	-	17:45:40.8487	-29:00:20.7756	12.89	15.01	172 $\times$ 111(138)	0.064 $\pm$ 0.013	0.375 $\pm$ 0.089	-	-	--
180	-	17:45:41.0156	-29:00:26.4324	12.92	15.38	115 $\times$ 55(25)	0.052 $\pm$ 0.014	0.138 $\pm$ 0.048	-	-	--
181	-	17:45:39.0811	-29:00:24.9056	12.95	9.40	240 $\times$ 0(33)	0.132 $\pm$ 0.013	0.493 $\pm$ 0.062	-	-	--
182	-	17:45:40.9475	-29:00:33.2946	13.02	13.35	296 $\times$ 189(10)	0.105 $\pm$ 0.011	1.531 $\pm$ 0.167	-	-	--
183	-	17:45:40.8918	-29:00:21.4103	13.03	13.63	184 $\times$ 140(97)	0.068 $\pm$ 0.013	0.517 $\pm$ 0.112	-	0.50 $\pm$ 0.026	- a
184	-	17:45:41.0282	-29:00:26.9501	13.03	36.77	661 $\times$ 253(162)	0.047 $\pm$ 0.006	1.962 $\pm$ 0.272	-	-	--
185	IRS 5	17:45:40.6956	-29:00:18.2766	13.05	0.84	81 $\times$ 59(171)	0.834 $\pm$ 0.014	1.823 $\pm$ 0.041	39.93 $\pm$ 1.986	372.26 $\pm$ 19.543	4 -
186	-	17:45:39.6933	-29:00:15.8245	13.05	18.29	138 $\times$ 60(147)	0.047 $\pm$ 0.013	0.152 $\pm$ 0.056	-	-	--
187	-	17:45:41.0380	-29:00:29.0877	13.15	31.11	100 $\times$ 18(30)	0.023 $\pm$ 0.014	0.044 $\pm$ 0.037	-	-	--
188	-	17:45:41.0381	-29:00:29.0851	13.16	32.15	109 $\times$ 23(31)	0.023 $\pm$ 0.014	0.048 $\pm$ 0.040	-	-	--
189	-	17:45:40.4343	-29:00:15.9412	13.19	20.95	178 $\times$ 97(36)	0.047 $\pm$ 0.013	0.258 $\pm$ 0.084	-	-	--
190	-	17:45:40.8112	-29:00:36.6198	13.26	4.02	212 $\times$ 145(11)	0.314 $\pm$ 0.013	2.682 $\pm$ 0.124	-	-	--
191	-	17:45:39.6948	-29:00:15.5601	13.30	13.57	126 $\times$ 88(133)	0.058 $\pm$ 0.013	0.225 $\pm$ 0.064	-	-	--
192	-	17:45:40.4536	-29:00:15.7828	13.44	9.66	153 $\times$ 123(131)	0.094 $\pm$ 0.013	0.543 $\pm$ 0.088	-	-	--
193	-	17:45:40.4519	-29:00:15.6462	13.56	17.36	243 $\times$ 182(168)	0.075 $\pm$ 0.012	0.883 $\pm$ 0.152	-	-	--
194	-	17:45:39.7399	-29:00:15.0726	13.57	12.17	266 $\times$ 46(66)	0.067 $\pm$ 0.013	0.418 $\pm$ 0.094	-	-	--
195	-	17:45:39.1642	-29:00:35.3859	13.60	16.27	520 $\times$ 337(84)	0.057 $\pm$ 0.006	2.500 $\pm$ 0.279	-	-	--

Table 6—Continued

ID	Alt Name	RA (J2000)	Dec (J2000)	Dist. from Sgr A*	Pos. Precision	$\theta_a \times \theta_b$ (PA)	Peak Intensity	Integrated Flux	Flux Ks	Flux L'	Refs & Comments
				( <i>arcsec</i> )	( <i>mas</i> )	<i>mas</i> $\times$ <i>mas</i> ( <i>deg</i> )	( <i>mJy beam</i> <sup>-1</sup> )	( <i>mJy</i> )	( <i>mJy</i> )	( <i>mJy</i> )	
196 -		17:45:41.0786	-29:00:25.8958	13.82	6.16	149 $\times$ 35(174)	0.162 $\pm$ 0.014	0.399 $\pm$ 0.045	-	-	--
197 -		17:45:41.0871	-29:00:26.5116	13.85	11.44	177 $\times$ 54(7)	0.098 $\pm$ 0.013	0.336 $\pm$ 0.058	-	-	--
198 -		17:45:41.0382	-29:00:32.6689	13.90	14.17	129 $\times$ 60(32)	0.058 $\pm$ 0.013	0.180 $\pm$ 0.053	-	-	--
199 -		17:45:38.9886	-29:00:30.2981	13.95	23.68	336 $\times$ 71(159)	0.077 $\pm$ 0.013	0.567 $\pm$ 0.109	-	-	--
200 -		17:45:41.0846	-29:00:30.8325	14.00	10.54	166 $\times$ 23(34)	0.089 $\pm$ 0.014	0.263 $\pm$ 0.051	-	-	--
201 -		17:45:40.4442	-29:00:15.0899	14.03	16.66	211 $\times$ 80(149)	0.069 $\pm$ 0.013	0.375 $\pm$ 0.084	-	-	--
202 -		17:45:40.4329	-29:00:14.9786	14.08	19.20	387 $\times$ 100(115)	0.053 $\pm$ 0.012	0.652 $\pm$ 0.155	-	-	--
203 -		17:45:39.0967	-29:00:34.9493	14.14	21.34	254 $\times$ 87(161)	0.067 $\pm$ 0.013	0.443 $\pm$ 0.099	-	-	--
204 -		17:45:41.1040	-29:00:25.6805	14.18	4.71	166 $\times$ 41(28)	0.209 $\pm$ 0.013	0.664 $\pm$ 0.054	-	-	--
205 -		17:45:41.1232	-29:00:29.1250	14.27	23.23	115 $\times$ 70(175)	0.036 $\pm$ 0.014	0.106 $\pm$ 0.052	-	-	--
206 -		17:45:41.1232	-29:00:29.1241	14.27	23.63	119 $\times$ 78(173)	0.036 $\pm$ 0.013	0.117 $\pm$ 0.056	-	-	--
207 n40		17:45:41.1055	-29:00:30.8395	14.27	13.37	216 $\times$ 89(31)	0.088 $\pm$ 0.013	0.526 $\pm$ 0.091	0.25 $\pm$ 0.013	0.24 $\pm$ 0.016	--
208 -		17:45:40.0734	-29:00:13.7723	14.30	9.08	203 $\times$ 51(128)	0.098 $\pm$ 0.013	0.453 $\pm$ 0.073	-	-	--
209 n41		17:45:41.0769	-29:00:23.4960	14.37	5.83	117 $\times$ 55(155)	0.138 $\pm$ 0.014	0.370 $\pm$ 0.048	0.27 $\pm$ 0.014	0.33 $\pm$ 0.018	--
210 -		17:45:39.0759	-29:00:35.0124	14.41	31.37	91 $\times$ 24(156)	0.023 $\pm$ 0.014	0.040 $\pm$ 0.035	-	-	--
211 -		17:45:41.1302	-29:00:25.1992	14.61	25.13	113 $\times$ 28(20)	0.032 $\pm$ 0.014	0.065 $\pm$ 0.039	-	-	--
212 -		17:45:41.1337	-29:00:25.4370	14.61	12.35	90 $\times$ 43(50)	0.052 $\pm$ 0.014	0.117 $\pm$ 0.042	-	-	--
213 -		17:45:41.0843	-29:00:33.1266	14.62	12.68	271 $\times$ 112(165)	0.121 $\pm$ 0.013	1.022 $\pm$ 0.122	-	-	--
214 -		17:45:41.0653	-29:00:33.8645	14.67	4.29	192 $\times$ 70(15)	0.271 $\pm$ 0.013	1.190 $\pm$ 0.070	-	-	--
215 -		17:45:41.1259	-29:00:24.6722	14.67	6.59	116 $\times$ 33(168)	0.128 $\pm$ 0.014	0.264 $\pm$ 0.040	-	-	--
216 -		17:45:41.1535	-29:00:26.5113	14.71	10.50	211 $\times$ 63(168)	0.120 $\pm$ 0.013	0.533 $\pm$ 0.071	-	-	--
217 -		17:45:41.1492	-29:00:30.1266	14.72	24.79	97 $\times$ 36(161)	0.030 $\pm$ 0.014	0.059 $\pm$ 0.038	-	-	--
218 -		17:45:41.1023	-29:00:23.2924	14.75	43.55	344 $\times$ 63(13)	0.044 $\pm$ 0.013	0.305 $\pm$ 0.103	-	-	--
219 -		17:45:41.1655	-29:00:30.1966	14.94	31.38	87 $\times$ 46(170)	0.023 $\pm$ 0.014	0.045 $\pm$ 0.039	-	-	--
220 -		17:45:41.1724	-29:00:26.5239	14.96	20.30	207 $\times$ 33(12)	0.062 $\pm$ 0.013	0.201 $\pm$ 0.055	-	-	--
221 -		17:45:41.1554	-29:00:24.9905	14.97	9.91	194 $\times$ 33(22)	0.115 $\pm$ 0.013	0.377 $\pm$ 0.056	-	-	--
222 -		17:45:41.1653	-29:00:25.1825	15.06	12.59	198 $\times$ 87(9)	0.095 $\pm$ 0.013	0.500 $\pm$ 0.081	-	-	--
223 -		17:45:40.0401	-29:00:12.9664	15.10	12.21	226 $\times$ 112(78)	0.067 $\pm$ 0.013	0.534 $\pm$ 0.116	-	-	--
224 -		17:45:39.1890	-29:00:38.2955	15.12	20.37	141 $\times$ 94(125)	0.039 $\pm$ 0.013	0.177 $\pm$ 0.072	-	-	--
225 -		17:45:41.1790	-29:00:25.6167	15.16	25.20	267 $\times$ 42(130)	0.043 $\pm$ 0.013	0.242 $\pm$ 0.086	-	-	--
226 n42		17:45:41.0923	-29:00:34.3266	15.18	5.38	123 $\times$ 50(88)	0.108 $\pm$ 0.013	0.351 $\pm$ 0.056	0.02 $\pm$ 0.004	0.12 $\pm$ 0.012	--
227 -		17:45:41.1862	-29:00:30.4889	15.25	20.83	177 $\times$ 125(14)	0.052 $\pm$ 0.013	0.335 $\pm$ 0.097	-	-	--
228 -		17:45:41.1769	-29:00:31.3529	15.29	4.59	99 $\times$ 53(10)	0.167 $\pm$ 0.014	0.383 $\pm$ 0.043	-	-	--
229 -		17:45:39.8997	-29:00:12.7857	15.39	15.36	181 $\times$ 163(133)	0.070 $\pm$ 0.013	0.584 $\pm$ 0.121	-	-	--
230 -		17:45:41.2218	-29:00:26.2774	15.63	24.91	217 $\times$ 82(6)	0.052 $\pm$ 0.013	0.284 $\pm$ 0.083	-	-	--
231 -		17:45:40.1043	-29:00:12.3756	15.72	9.92	67 $\times$ 0(125)	0.055 $\pm$ 0.014	0.065 $\pm$ 0.028	-	-	--
232 -		17:45:41.1192	-29:00:34.8645	15.72	13.62	483 $\times$ 168(10)	0.136 $\pm$ 0.009	2.829 $\pm$ 0.196	-	-	--
233 -		17:45:39.6412	-29:00:13.2314	15.73	5.57	263 $\times$ 82(98)	0.125 $\pm$ 0.013	0.973 $\pm$ 0.114	-	-	--
234 -		17:45:41.0937	-29:00:20.5394	15.76	33.52	181 $\times$ 85(179)	0.034 $\pm$ 0.013	0.160 $\pm$ 0.075	-	-	--
235 n43		17:45:40.4774	-29:00:13.3632	15.79	24.70	196 $\times$ 122(50)	0.040 $\pm$ 0.013	0.288 $\pm$ 0.106	23.80 $\pm$ 1.205	43.22 $\pm$ 2.269	--
236 -		17:45:40.4777	-29:00:13.3583	15.80	24.97	262 $\times$ 136(66)	0.040 $\pm$ 0.013	0.418 $\pm$ 0.144	-	-	--
237 -		17:45:41.0718	-29:00:36.1862	15.80	12.91	457 $\times$ 347(150)	0.095 $\pm$ 0.007	3.756 $\pm$ 0.265	-	-	--
238 -		17:45:41.1233	-29:00:35.0698	15.86	6.49	172 $\times$ 0(27)	0.158 $\pm$ 0.014	0.404 $\pm$ 0.046	-	-	--
239 -		17:45:41.2339	-29:00:30.8441	15.93	11.33	242 $\times$ 77(45)	0.098 $\pm$ 0.013	0.629 $\pm$ 0.096	-	-	--
240 -		17:45:41.2613	-29:00:27.4785	16.05	16.12	111 $\times$ 53(170)	0.051 $\pm$ 0.014	0.124 $\pm$ 0.045	-	-	--
241 -		17:45:41.2584	-29:00:25.6813	16.18	13.86	215 $\times$ 64(158)	0.089 $\pm$ 0.013	0.413 $\pm$ 0.073	-	-	--
242 -		17:45:41.2625	-29:00:26.1201	16.18	14.51	111 $\times$ 44(141)	0.050 $\pm$ 0.014	0.125 $\pm$ 0.045	-	-	--
243 -		17:45:41.2612	-29:00:25.4845	16.25	5.51	88 $\times$ 60(153)	0.128 $\pm$ 0.014	0.303 $\pm$ 0.044	-	-	--
244 -		17:45:41.2571	-29:00:25.0159	16.28	8.86	208 $\times$ 0(147)	0.126 $\pm$ 0.014	0.361 $\pm$ 0.050	-	-	--

Table 6—Continued

ID	Alt Name	RA (J2000)	Dec (J2000)	Dist. from Sgr A* (arcsec)	Pos. Precision (mas)	$\theta_a \times \theta_b$ (PA) mas $\times$ mas (deg)	Peak Intensity (mJy beam <sup>-1</sup> )	Integrated Flux (mJy)	Flux Ks (mJy)	Flux L' (mJy)	Refs & Comments
245	-	17:45:41.2769	-29:00:26.0669	16.37	15.63	93 $\times$ 0(143)	0.043 $\pm$ 0.014	0.067 $\pm$ 0.033	-	-	--
246	-	17:45:38.8232	-29:00:23.9115	16.47	17.78	157 $\times$ 91(43)	0.050 $\pm$ 0.013	0.237 $\pm$ 0.075	-	-	--
247	-	17:45:41.2790	-29:00:25.5622	16.47	11.69	158 $\times$ 37(135)	0.070 $\pm$ 0.013	0.228 $\pm$ 0.055	-	-	--
248	-	17:45:41.2756	-29:00:25.2239	16.48	17.39	250 $\times$ 39(4)	0.086 $\pm$ 0.013	0.338 $\pm$ 0.064	-	-	--
249	-	17:45:41.2935	-29:00:25.2157	16.71	28.60	288 $\times$ 46(134)	0.043 $\pm$ 0.013	0.261 $\pm$ 0.091	-	-	--
250	-	17:45:41.2080	-29:00:34.6999	16.72	12.44	150 $\times$ 24(134)	0.064 $\pm$ 0.014	0.185 $\pm$ 0.051	-	-	--
251	-	17:45:41.3025	-29:00:25.5407	16.78	18.19	196 $\times$ 66(142)	0.057 $\pm$ 0.013	0.265 $\pm$ 0.074	-	-	--
252	-	17:45:39.0071	-29:00:18.0328	16.84	27.97	340 $\times$ 122(11)	0.064 $\pm$ 0.012	0.720 $\pm$ 0.149	-	-	--
253	-	17:45:38.8514	-29:00:34.6366	16.90	32.01	266 $\times$ 26(151)	0.044 $\pm$ 0.013	0.187 $\pm$ 0.068	-	-	--
254	-	17:45:40.7495	-29:00:13.9038	16.96	10.84	383 $\times$ 258(118)	0.097 $\pm$ 0.008	2.463 $\pm$ 0.215	-	-	--
255	-	17:45:41.2210	-29:00:34.9159	16.96	7.13	55 $\times$ 33(11)	0.087 $\pm$ 0.014	0.127 $\pm$ 0.032	-	-	--
256	-	17:45:41.3178	-29:00:25.2774	17.02	30.85	261 $\times$ 67(174)	0.050 $\pm$ 0.013	0.270 $\pm$ 0.084	-	-	--
257	-	17:45:39.7111	-29:00:11.4971	17.12	15.44	159 $\times$ 70(74)	0.043 $\pm$ 0.013	0.196 $\pm$ 0.072	-	-	--
258	-	17:45:41.3240	-29:00:24.9570	17.15	6.88	24 $\times$ 0(3)	0.064 $\pm$ 0.015	0.058 $\pm$ 0.024	-	-	--
259	-	17:45:41.2972	-29:00:32.7643	17.17	11.04	156 $\times$ 93(33)	0.085 $\pm$ 0.013	0.400 $\pm$ 0.074	-	-	--
260	-	17:45:41.3409	-29:00:26.1492	17.20	22.75	152 $\times$ 0(152)	0.041 $\pm$ 0.014	0.082 $\pm$ 0.039	-	-	--
261	n44	17:45:39.7365	-29:00:11.3046	17.23	7.82	324 $\times$ 118(97)	0.099 $\pm$ 0.012	1.160 $\pm$ 0.152	0.16 $\pm$ 0.011	0.27 $\pm$ 0.018	--
262	-	17:45:39.3426	-29:00:42.7085	17.25	7.62	217 $\times$ 24(115)	0.095 $\pm$ 0.013	0.437 $\pm$ 0.073	0.05 $\pm$ 0.003	-	- b
263	-	17:45:41.3483	-29:00:25.5177	17.37	16.52	164 $\times$ 43(3)	0.065 $\pm$ 0.014	0.186 $\pm$ 0.050	-	-	--
264	-	17:45:39.3112	-29:00:42.6938	17.46	11.26	403 $\times$ 375(167)	0.104 $\pm$ 0.007	3.916 $\pm$ 0.259	-	-	--
265	-	17:45:41.3648	-29:00:26.3373	17.49	28.58	250 $\times$ 0(142)	0.043 $\pm$ 0.014	0.117 $\pm$ 0.049	-	-	--
266	-	17:45:38.8057	-29:00:21.1645	17.58	14.10	118 $\times$ 82(50)	0.053 $\pm$ 0.013	0.191 $\pm$ 0.060	-	-	--
267	-	17:45:41.3607	-29:00:24.6881	17.67	7.90	-	0.055 $\pm$ 0.015	0.037 $\pm$ 0.019	-	-	--
268	-	17:45:41.3704	-29:00:25.2665	17.70	11.58	61 $\times$ 23(2)	0.056 $\pm$ 0.014	0.076 $\pm$ 0.030	-	-	--
269	-	17:45:38.8066	-29:00:20.6206	17.79	15.78	168 $\times$ 107(35)	0.062 $\pm$ 0.013	0.344 $\pm$ 0.085	-	-	--
270	-	17:45:39.2095	-29:00:13.9728	17.80	18.67	133 $\times$ 91(12)	0.048 $\pm$ 0.013	0.190 $\pm$ 0.065	-	-	--
271	-	17:45:38.9316	-29:00:38.8503	18.08	11.97	170 $\times$ 121(8)	0.089 $\pm$ 0.013	0.538 $\pm$ 0.091	0.05 $\pm$ 0.003	-	- b
272	-	17:45:39.0639	-29:00:40.9216	18.13	14.91	237 $\times$ 64(168)	0.093 $\pm$ 0.013	0.458 $\pm$ 0.077	-	-	--
273	-	17:45:41.3908	-29:00:24.1526	18.17	18.63	184 $\times$ 87(15)	0.060 $\pm$ 0.013	0.299 $\pm$ 0.077	-	-	--
274	-	17:45:38.7984	-29:00:36.1891	18.18	22.13	210 $\times$ 102(4)	0.057 $\pm$ 0.013	0.358 $\pm$ 0.094	-	-	--
275	-	17:45:41.4132	-29:00:24.9639	18.30	27.23	227 $\times$ 119(154)	0.047 $\pm$ 0.013	0.359 $\pm$ 0.113	-	-	--
276	-	17:45:38.7295	-29:00:21.2475	18.47	17.47	122 $\times$ 65(37)	0.045 $\pm$ 0.013	0.142 $\pm$ 0.054	-	-	--
277	-	17:45:41.4179	-29:00:23.9070	18.57	42.25	185 $\times$ 92(173)	0.027 $\pm$ 0.013	0.138 $\pm$ 0.080	-	-	--
278	-	17:45:38.6543	-29:00:23.4128	18.74	19.64	302 $\times$ 73(7)	0.088 $\pm$ 0.013	0.588 $\pm$ 0.099	-	-	--
279	-	17:45:38.7615	-29:00:19.4502	18.84	15.84	61 $\times$ 41(93)	0.036 $\pm$ 0.014	0.066 $\pm$ 0.037	-	-	--
280	-	17:45:41.4322	-29:00:23.3200	18.89	41.46	272 $\times$ 116(134)	0.030 $\pm$ 0.013	0.277 $\pm$ 0.133	-	-	--
281	-	17:45:41.4879	-29:00:27.0501	19.04	28.21	525 $\times$ 140(169)	0.074 $\pm$ 0.009	1.418 $\pm$ 0.189	-	-	--
282	-	17:45:41.3694	-29:00:20.3179	19.10	17.07	169 $\times$ 29(119)	0.041 $\pm$ 0.013	0.150 $\pm$ 0.061	-	-	--
283	-	17:45:41.3320	-29:00:19.1094	19.19	17.87	120 $\times$ 0(137)	0.041 $\pm$ 0.014	0.089 $\pm$ 0.042	-	-	--
284	-	17:45:41.4605	-29:00:22.7906	19.39	26.27	337 $\times$ 155(155)	0.058 $\pm$ 0.011	0.804 $\pm$ 0.164	-	-	--
285	-	17:45:38.6289	-29:00:34.3247	19.52	12.00	193 $\times$ 75(129)	0.075 $\pm$ 0.013	0.388 $\pm$ 0.080	-	-	--
286	-	17:45:41.4983	-29:00:23.4224	19.71	33.76	311 $\times$ 114(163)	0.051 $\pm$ 0.013	0.500 $\pm$ 0.140	-	-	--
287	n45	17:45:41.5337	-29:00:26.0544	19.72	26.84	181 $\times$ 103(54)	0.034 $\pm$ 0.013	0.201 $\pm$ 0.091	0.14 $\pm$ 0.008	0.12 $\pm$ 0.008	--
288	-	17:45:38.6881	-29:00:19.1668	19.82	23.82	244 $\times$ 169(57)	0.046 $\pm$ 0.012	0.529 $\pm$ 0.150	-	-	--
289	-	17:45:41.5089	-29:00:23.0871	19.92	18.00	143 $\times$ 45(14)	0.053 $\pm$ 0.014	0.144 $\pm$ 0.049	-	-	--
290	-	17:45:41.4152	-29:00:19.4268	20.02	34.72	209 $\times$ 74(50)	0.028 $\pm$ 0.013	0.153 $\pm$ 0.085	-	-	--
291	-	17:45:41.4263	-29:00:19.6998	20.04	12.41	124 $\times$ 0(60)	0.042 $\pm$ 0.015	0.000 $\pm$ 0.002	-	-	--
292	-	17:45:38.5017	-29:00:27.0224	20.19	19.61	68 $\times$ 0(169)	0.034 $\pm$ 0.014	0.042 $\pm$ 0.029	-	-	--
293	-	17:45:38.8490	-29:00:15.2240	20.21	9.25	116 $\times$ 95(78)	0.080 $\pm$ 0.013	0.313 $\pm$ 0.064	-	-	--

Table 6—Continued

ID	Alt Name	RA (J2000)	Dec (J2000)	Dist. from Sgr A* (arcsec)	Pos. Precision (mas)	$\theta_a \times \theta_b$ (PA) mas $\times$ mas (deg)	Peak Intensity (mJy beam <sup>-1</sup> )	Integrated Flux (mJy)	Flux Ks (mJy)	Flux L' (mJy)	Refs & Comments
294	-	17:45:41.5584	-29:00:31.6049	20.25	9.42	232 $\times$ 65(57)	0.097 $\pm$ 0.013	0.574 $\pm$ 0.090	-	-	--
295	-	17:45:41.4205	-29:00:19.0474	20.25	31.72	175 $\times$ 33(145)	0.031 $\pm$ 0.013	0.098 $\pm$ 0.055	-	-	--
296	-	17:45:41.5332	-29:00:22.5257	20.38	13.58	142 $\times$ 73(178)	0.070 $\pm$ 0.013	0.246 $\pm$ 0.059	-	-	--
297	-	17:45:41.2010	-29:00:14.3333	20.53	10.14	126 $\times$ 45(133)	0.072 $\pm$ 0.014	0.206 $\pm$ 0.050	-	-	--
298	-	17:45:41.4398	-29:00:18.3367	20.80	68.39	293 $\times$ 99(177)	0.025 $\pm$ 0.013	0.202 $\pm$ 0.119	-	-	--
299	-	17:45:41.5803	-29:00:22.3161	21.03	15.00	181 $\times$ 74(110)	0.048 $\pm$ 0.013	0.245 $\pm$ 0.080	-	-	--
300	-	17:45:41.4498	-29:00:18.0416	21.06	17.46	196 $\times$ 105(115)	0.049 $\pm$ 0.013	0.324 $\pm$ 0.099	-	-	--
301	-	17:45:38.6411	-29:00:17.5982	21.11	17.81	395 $\times$ 338(48)	0.063 $\pm$ 0.007	2.132 $\pm$ 0.245	-	-	--
302	-	17:45:39.9124	-29:00:49.3133	21.31	9.83	149 $\times$ 127(126)	0.092 $\pm$ 0.013	0.533 $\pm$ 0.089	-	-	--
303	-	17:45:38.5850	-29:00:37.7890	21.40	31.64	370 $\times$ 74(136)	0.050 $\pm$ 0.013	0.459 $\pm$ 0.132	-	-	--
304	-	17:45:41.6042	-29:00:21.8618	21.46	12.82	102 $\times$ 53(12)	0.060 $\pm$ 0.014	0.141 $\pm$ 0.043	-	-	--
305	-	17:45:38.8451	-29:00:13.3551	21.48	19.04	228 $\times$ 76(13)	0.070 $\pm$ 0.013	0.379 $\pm$ 0.083	-	-	--
306	-	17:45:41.6864	-29:00:19.8473	23.13	16.92	187 $\times$ 57(32)	0.061 $\pm$ 0.013	0.251 $\pm$ 0.066	-	0.33 $\pm$ 0.017	- a
307	-	17:45:41.7140	-29:00:19.2837	23.67	9.00	166 $\times$ 125(137)	0.107 $\pm$ 0.013	0.666 $\pm$ 0.094	-	-	--
308	-	17:45:38.2814	-29:00:21.9344	23.85	20.57	198 $\times$ 56(19)	0.057 $\pm$ 0.013	0.229 $\pm$ 0.066	-	-	--
309	-	17:45:41.8513	-29:00:30.2155	23.88	19.05	487 $\times$ 371(94)	0.052 $\pm$ 0.006	2.357 $\pm$ 0.283	-	-	--
310	-	17:45:38.2666	-29:00:21.6713	24.11	26.77	158 $\times$ 56(169)	0.038 $\pm$ 0.013	0.123 $\pm$ 0.055	-	-	--
311	-	17:45:41.8561	-29:00:23.6745	24.25	25.51	296 $\times$ 106(25)	0.062 $\pm$ 0.013	0.559 $\pm$ 0.129	-	-	--
312	-	17:45:41.7261	-29:00:17.8341	24.39	28.63	208 $\times$ 70(170)	0.044 $\pm$ 0.013	0.204 $\pm$ 0.074	-	-	--
313	-	17:45:41.4663	-29:00:11.6292	24.92	8.68	4 $\times$ 0(9)	0.056 $\pm$ 0.015	0.049 $\pm$ 0.023	-	-	--
314	-	17:45:41.8096	-29:00:17.9834	25.33	24.39	306 $\times$ 109(128)	0.051 $\pm$ 0.013	0.510 $\pm$ 0.142	-	-	--
315	-	17:45:37.8554	-29:00:26.1322	28.70	21.10	225 $\times$ 47(9)	0.064 $\pm$ 0.013	0.254 $\pm$ 0.065	-	-	--
316	-	17:45:40.1361	-28:59:58.8907	29.21	9.45	-	0.043 $\pm$ 0.015	0.005 $\pm$ 0.007	-	-	--
317	-	17:45:40.1236	-28:59:58.1925	29.90	9.61	119 $\times$ 88(70)	0.075 $\pm$ 0.013	0.290 $\pm$ 0.063	-	-	--
318	-	17:45:38.8944	-29:00:57.8753	33.37	11.38	246 $\times$ 88(146)	0.112 $\pm$ 0.013	0.749 $\pm$ 0.100	-	-	--
-											

Note. — **References:** 1 - Viehmann et al. (2005); 2 - Eckart et al. (2004); 3 - Paumard et al. (2006) and 4 - Moulataka et al. (2009). **Comments:** a - Detected only in  $L'$ ; b - Detected only in  $K_s$  and faint source.